工學博士學位論文

High-Performance Perovskite Solar Cells Using Solution-Processable Polyaniline Hole Transport Materials

용액공정이 가능한 폴리아닐린 기반의 홀 전달물질을 사용한 고성능 페로브스카이트 태양전지 제조

2019年 2月

서울大學校 大學院

化學生物工學部

李 錡 秀

High-Performance Perovskite Solar Cells Using Solution-Processable Polyaniline Hole Transport Materials

by

Kisu Lee

Submitted to the Graduate School of Seoul National University in Partial Fulfillment of the Requirements for the Degree of Doctor of Philosophy

February, 2019

Thesis Adviser: Jyongsik Jang

Abstract

Perovskite solar cells (PSCs) based on organic-inorganic hybrid perovskite materials have developed rapidly as one of the most promising next generation photovoltaics. Along with perovskite absorber materials, charge transport materials have a critical influence on photovoltaic performance and stability of the devices. In generally, organic small molecule, conducting polymer, and metal oxide semiconductors are employed as charge transport layer in PSCs. Among them, conducting polymers have numerous advantages compared to other semiconductors so they have attracted great attention. In contrast to metal oxides, conducting polymers can be processed at a low temperature, indicating a possibility to fabricate flexible devices on plastic substrates. Furthermore, they are processed from solution, and can be simply deposited by solution processing methods such as spin-coating and spraying. They also produce thin films with less defects than organic small molecules due to better film forming properties. However, conducting polymers that have been generally used for PSCs are expensive and can increase the overall device cost.

Polyaniline (PANI), a representative conducting polymer, has been

widely used in electronic applications of organic light-emitting diodes (OLEDs), dye-sensitized solar cells (DSSCs), electrochromic devices, and sensor applications due to its simple synthesis, good conductivity, and environmental stability. Especially, aniline, which is the monomer of PANI, is much cheaper than that of other conducting polymers for PSCs, including poly(3,4-ethylenedioxythiophene) (PEDOT), poly(3-hexylthiophene-2,5-diyl) (P3HT), and poly(triaryl amine) (PTAA). Thus, PANI has great potential as an alternative charge transport material in PSC applications. There have been a few studies on PANI-based charge transport material in PSCs, but the fabricated devices showed poor photovoltaic performances or required complex, unreproducible synthetic methods.

This dissertation describes the effective synthetic and application methods of PANI-based charge transport materials for different PSC structures. Solution-processable PANI was synthesized and utilized as a hole transport layer (HTL) in inverted and carbon electrode-based PSC. Firstly, water-dispersible polyaniline:poly(styrenesulfonate) (PANI:PSS) was synthesized and modified with a surfactant to improve its hole transport ability. Triton X–100, which is added to PANI:PSS dispersion, induced better wettability and favorable surface

composition. The surfactant-modified PANI:PSS resulted in improvements of photovoltaic performance of inverted PSCs. Secondly, polyaniline doped with camphorsulfonic acid (PANI-CSA) was utilized as an HTL in inverted PSCs and the resulting devices were compared with those using PEDOT:PSS, which is the most used HTL. PANI-CSA showed superior hole transport ability to PEDOT:PSS due to its better conductivity and charge mobility, leading to a higher device efficiency. Moreover, the fabricated PSCs showed significantly improved ambient stability by replacing hygroscopic PEDOT:PSS with moisture-resistant PANI-CSA. Finally, PANI-CSA was also introduced to HTL in carbon electrode-based PSCs. PANI-CSA dispersed in organic solvents rarely degrades perovskite thus could be deposited onto perovskite layer. The inserted PANI-CSA layer effectively suppressed undesirable charge recombination at perovskite/carbon electrode interface, and improved photovoltaic performances. The resulting devices were highly stable under humid and heating conditions due to moisture- and thermally stable PANI-CSA and carbon layers. The fabricated PANI-based hole transport materials are efficient, stable, and versatile. Accordingly, this study provides synthetic and application approaches of conducting

polymer PANI as hole transport material to achieve low-cost, efficient, stable, and flexible perovskite optoelectronics.

Keywords: Perovskite solar cell, Conducting polymer, Polyaniline, Hole transport material, Carbon electrode.

Student Number: 2016-30234

List of Abbreviations

A: active area

AFM: Atomic force microscopy

AM: air mass coefficient

cETL: compact electron transport layer

CSA: camphorsulfonic acid

CV: cyclic voltammetry

d: thickness

DC: direct current

DI: deionized

DMF: dimethylformamide

DMSO: dimethyl sulfoxide

EB: emeraldine base

EDX: energy-dispersive X-ray

EIS: electrochemical impedance spectroscopy

EQE: external quantum efficiency

ES: emeraldine salt

ETL: electron transport layer

ETM: electron transport material

FA: formamidinium

FE-SEM: field emission-scanning electron microscopy

FF: fill factor

FTO: fluorine-doped tin oxide

h: hour

HOMO: highest occupied molecular orbital

HTL: hole transport layer

HTM: hole transport material

IPCE: incident photon-to-current efficiency

ITO: indium tin oxide

I–V: current–voltage

J_{SC}: short-circuit current density

J–V: current density–voltage

Li-TFSI: lithium bis(trifluoromethylsulphonyl)imide

LUMO: lowest unoccupied molecular orbital

MA: methylammonium

mETL: mesoporous electron transport layer

mg: miligram

min: minute

mL: milliliter

nm: nanometer

PANI: polyaniline

PANI-CSA: polyaniline doped with camphorsulfonic acid

PANI:PSS: polyaniline:poly(styrenesulfonate)

PCBM: Phenyl-C61-butyric acid methyl ester

PCE: power conversion efficiency

PEDOT:PSS: poly(3,4-ethylenedioxythiophene):poly(styrene-sulfonate)

PET: polyethylene terephthalate

PL: photoluminescence

PSC: perovskite solar cell

PSS: poly(styrenesulfonate)

PTAA: poly(triaryl amine)

R_{CT}: charge transfer resistance

R_{REC}: charge recombination resistance

R_S: series resistance

s: second

SCLC: space-charge-limited current

s-PANI:PSS: surfactant-modified polyaniline:poly(styrenesulfonate)

spiro-OMeTAD: 2,2′,7,7′-tetrakis(N,N-di-p-methoxyphenylamine)-

9,9′-spirobifluorene

SSDP: self-stabilized dispersion polymerization

TCO: transparent conductive oxide

UPS: ultraviolet photoelectron spectroscopy

UV-VIS: ultraviolet–visible

UVO: ultraviolet–ozone

V_{OC}: open-circuit voltage

w/o: without

XRD: X-ray diffraction

μm: micrometer

ε: relative dielectric constant

ε_0: free space permittivity

η: efficiency

θ: theta

μ: charge mobility

σ_0: direct current conductivity

τ: photoluminescence lifetime

List of Figures

List of Tables

Table of Contents

1. Introduction

1.1 Background

1.1.1. Perovskite solar cells

Perovskite solar cells (PSCs) based on organic-inorganic hybrid perovskite material have attracted the great attention as the most promising next-generation photovoltaic technology [1,2]. A typical perovskite has three-dimensional (3D) ABX_3 structure as shown in **Figure 1** where A is composed of organic or inorganic cation (CH_3NH_3 (MA), $CH(NH_2)_2$ (FA), and Cs), b is the divalent metal (Pb and Sn), and X is halide anion (Cl, Br, and I) [3]. PSCs have a huge potential for a high power conversion efficiency (PCE) due to excellent optoelectronic properties of the perovskite absorber material. Perovskite materials have appropriate band gap energy about 1.6 eV, which can absorb the complete visible solar spectrum [4,5]. A high absorption coefficient and a low exciton binding energy enable the perovskite materials to produce more photo-generated excitons. In addition, the excited charge carriers can be collected efficiently due to a high carrier mobility and a long charge diffusion length [6,7]. With tremendous developments of processing [8], compositional [9,10], and

interfacial engineering methods [11], PSCs have achieved a certified PCE over 20% [12]. **Figure 2** illustrates summary of various engineering methods to improve photovoltaic performance of PSCs.

Generally, device structure can be classified into three types depending on their component layers and charge transport direction: (1) meso-structured PSCs which composed of transparent conductive oxide (TCO)/compact electron transport layer (cETL)/mesoporous electron transport layer (mETL)/perovskite/hole transport layer (HTL)/metal, (2) ‘‘n–i–p’’ planar PSCs which composed of TCO/cETL/perovskite/HTL/metal, and (3) inverted ‘‘p–i–n’’ planar PSCs which composed of TCO/HTL/perovskite/ETL/metal [13]. Schematic illustrations in **Figure 3** show the device structures explained above.

Although PSCs have achieved significant progress in PCE rivaling that of crystalline silicon solar cells, there are critical hurdles that hinder their commercialization. According to many previous reports, perovskite materials are unstable under exposure to moisture and oxygen in ambient air, heat, and light [14]. Therefore, many researchers have focused on the stability issues of perovskite materials. Representatively, development of perovskite composition from

$MAPbI_3$ to triple-cation perovskite $Cs_xMA_yFA_{1-x-y}Pb(I_{1-z}Br_z)_3$ considerably improve both device efficiency and stability [10]. Recently, low dimensional perovskite materials have attracted much attention since they are highly stable against moisture and thermal stress [15,16]. Combination of conventional perovskite and low dimensional perovskite is regarded as a promising venue to realize stable perovskite absorber material [17]. However, degradation of device performance can be originated from not only perovskite itself, but also charge transport and electrode materials [18]. Thus, development of alternative charge transport material with high stability is important to achieve stable PSCs.

Apart from the stability, process and material costs are also challenging issue for the commercialization. Metal oxides used as charge transport layer including TiO_2, ZnO, and NiO require high-temperature sintering process over 300 °C. This process increases fabrication time and cost. Expensive charge transport materials, including 2,2′,7,7′-tetrakis(N,N-di-p-methoxyphenylamine)-9,9′-spirobifluorene (spiro-OMeTAD) and poly(triaryl amine) (PTAA), and novel metals, including gold (Au) and silver (Ag) also increase the overall device cost. Consequently, it is highly desired to develop

stable, low-cost, and efficient charge transport material for commercialization of PSCs.

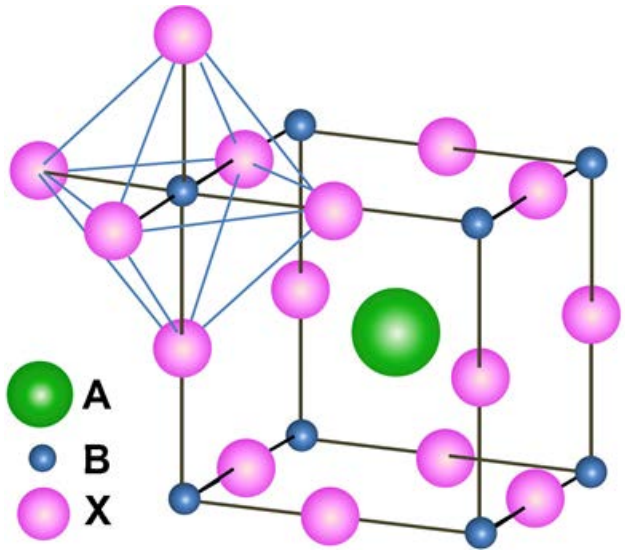

Figure 1. Schematic illustration of ABX_3 perovskite structure [3].

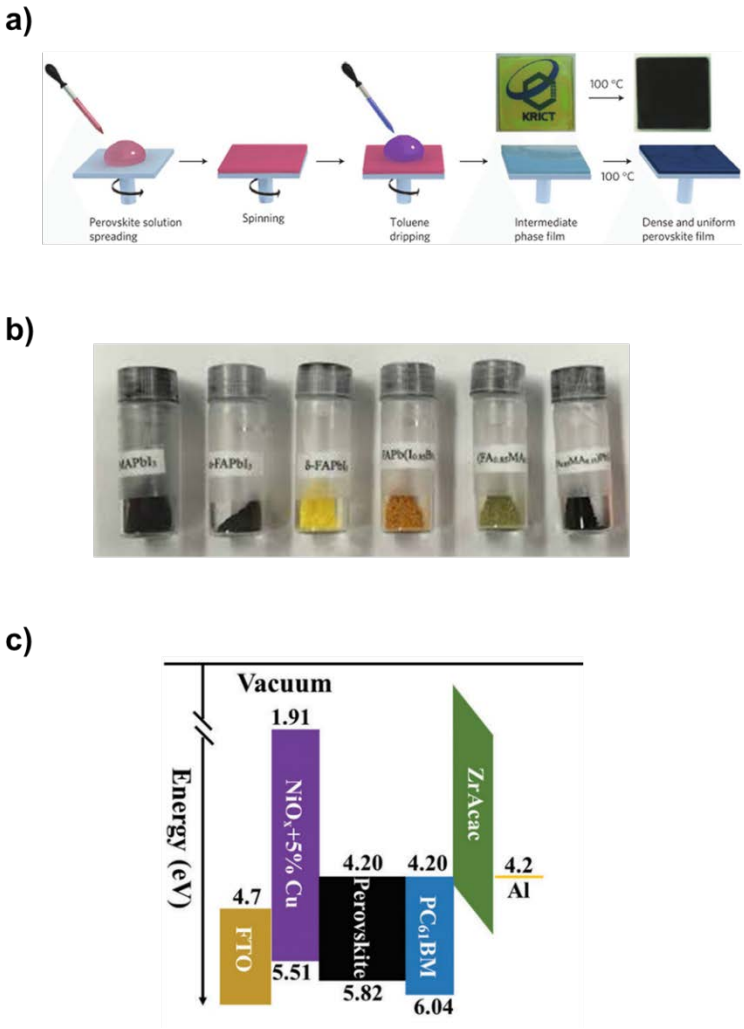

Figure 2. Various engineering methods of PSCs: (a) solvent engineering, (b) compositional engineering, and (c) interfacial engineering [8,9,11].

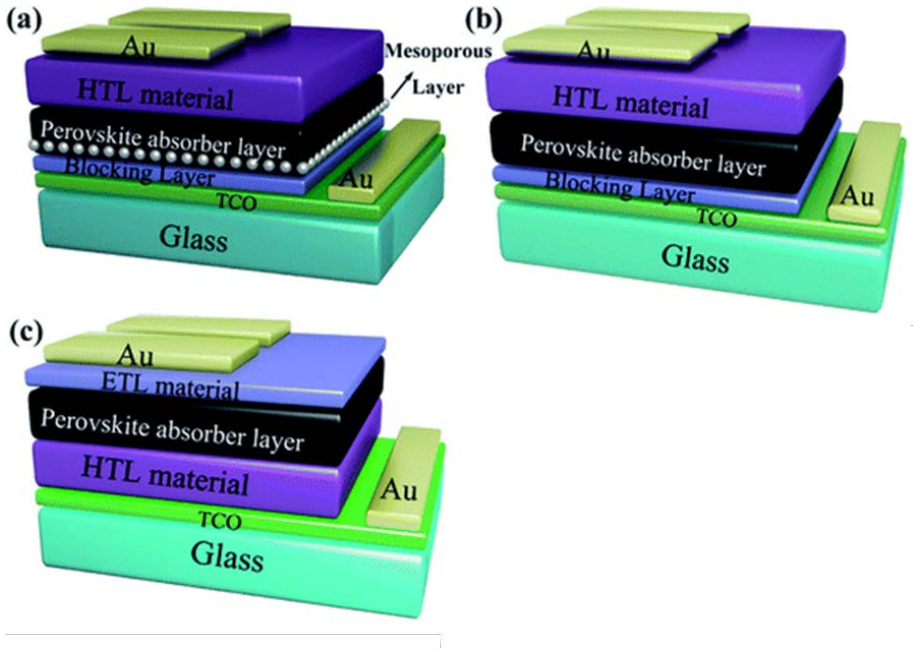

Figure 3. Schematic illustration of the device structures: (a) meso-structured structure, (b) planar structure, and (c) inverted structure [13].

1.1.1.1. Inverted perovskite solar cells

Although mesoscopic PSCs with TiO_2 layers have achieved over 20% PCE, complex processes including repeated high-temperature sintering process (>450 °C) have limited the scale-up manufacture and also eliminated the potential for tandem and flexible devices [19]. Therefore, p–i–n type planar PSCs, the so-called “inverted” PSCs, are attracting more attention as an alternative architecture. The inverted PSCs have a typical structure of a TCO/HTL/perovskite/ETL/metal. A fullerene derivative phenyl-C61-butyric acid methyl ester (PCBM) is generally used as the ETL due to its high electron mobility and solubility in non-polar solvents. Due to the passivation effect of PCBM, inverted PSCs show much less hysteresis behavior in the current density–voltage (*J*–*V*) characteristic curves than n–i–p type PSCs [20]. For a HTL, a conducting polymer, such as poly(3,4-ethylenedioxythiophene):poly(styrene-sulfonate) (PEDOT:PSS) or PTAA, and metal oxide such as NiO are employed. The appropriate alignment of valence level of NiO with that of the perovskite produce high open-circuit voltage devices but it requires the high-temperature sintering process of over 300 °C [21]. Therefore, conducting polymers

are promising hole transport materials (HTMs) to realize low-temperature processed and flexible inverted PSCs.

1.1.1.2. Carbon electrode-based perovskite solar cells

Device degradations originated from HTM and metal electrode (e.g. Au and Ag) are concerned issues in PSCs. The most commonly used organic small molecule spiro-OMeTAD with hygroscopic lithium bis(trifluoromethylsulphonyl)imide (Li-TFSI) dopant as HTM seriously destroys the ambient and thermal stabilities of PSCs [22]. Corrosion of metal electrodes by diffused halogen ions also causes the device degradation [23]. Additionally, expensive spiro-OMeTAD and novel metals significantly increase the device cost.

Therefore, carbon electrode-based PSCs without HTM is an ideal architecture to realize low-cost and stable device. There are two types of carbon electrode-based device: A fully printable device with architecture of TCO/cETL/mETL/Al_2O_3 or ZrO_2/carbon (**Figure 4a**) nd paintable carbon electrode-based device with architecture of TCO/cETL/mETL/perovskite/carbon (**Figure 4b**) [24]. Fully printable PSCs are usually fabricated by drop-casting the perovskite precursor solution on sequentially deposited TiO_2/Al_2O_3 or ZrO_2/carbon layers. This method requires the complex structure and high-temperature fabrication processes. Moreover, restricted perovskite growth within the multi-layer mesoporous structure can result in small, non-uniform

perovskite grains, which might be detrimental to photovoltaic performance. In paintable carbon electrode-based PSCs, the carbon electrode is deposited using doctor blading or screen-printing on the fluorine-doped tin oxide (FTO)/compact TiO_2/mesoporous TiO_2/perovskite as prepared in the conventional devices. This method can make use of highly crystalline perovskite films, thus have a huge potential for high PCE. However, interfacial charge recombination at perovskite/carbon due to the absence of HTM seriously deteriorates the device efficiency [24,25]. Thus, it is required to suppress interfacial charge recombination for efficient and highly stable carbon electrode-based PSCs.

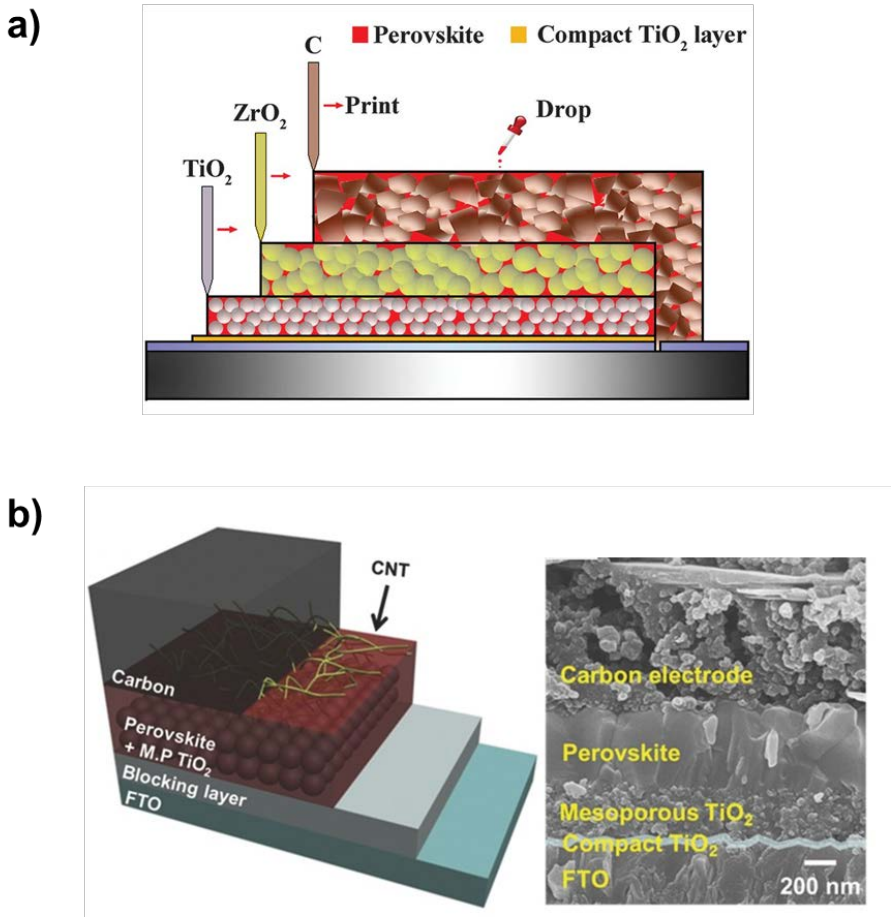

Figure 4. Schematic illustration and image of device architectures of (a) a fully printable PSC and (b) a paintable carbon electrode-based PSC. [26,27].

1.1.2.2. Conducting polymers

Over the past several decades, conducting polymers have received much attention as the replacement for inorganic materials or metals due to low cost, light weight, good processability, ease of synthesis, mechanical flexibility, and broad functionalization capability. Since the discovery of highly conductive polyacetylene (PA) in 1977, various conducting polymers, such as poly(3,4-ethylenedioxythiophene) (PEDOT), polyaniline (PANI), polypyrrole (PPy), polythiophene (PT), and poly(*p*-phenylene vinylene) (PPV), have been investigated as an electronic material (**Figure 5**).

In general, conducting polymers have alternating single (σ) and double (π) bonds, and the highly conjugated system induces unique optical, electrical, and electrochemical properties [28]. However, to obtain electrical conductivity, further chemical treatment, which is called “doping”, is required. The electrical conductivity of conducting polymers can be controlled over the full range of insulator, semiconductor, and metal, by doping [29]. In this process, doping agents, that can add electrons (n-doping) or remove electrons (p-doping), are introduced to the polymer so that charge carriers can move along the polymer chain [28]. Doping process is carried out by a redox

reaction or an acid-base reaction, and it is reversible process which can revert to the original state without degradation of the polymer backbone. During doping and dedoping processes, dopant counter-ions are involved to maintain the charge neutrality. The doping is the unique and underlying concept, distinguishing conducting polymers from all other polymers, and results in dramatic changes in the electronic, electrical, optical, and structural properties [30].

Due to the many advantages as a polymer and unique chemical/electrochemical properties, conducting polymers have been widely studied in applications including transistors, batteries, light-emitting diodes (LED), sensors, antistatic coatings, fuel cells, solar cells, and supercapacitors (**Figure 6**).

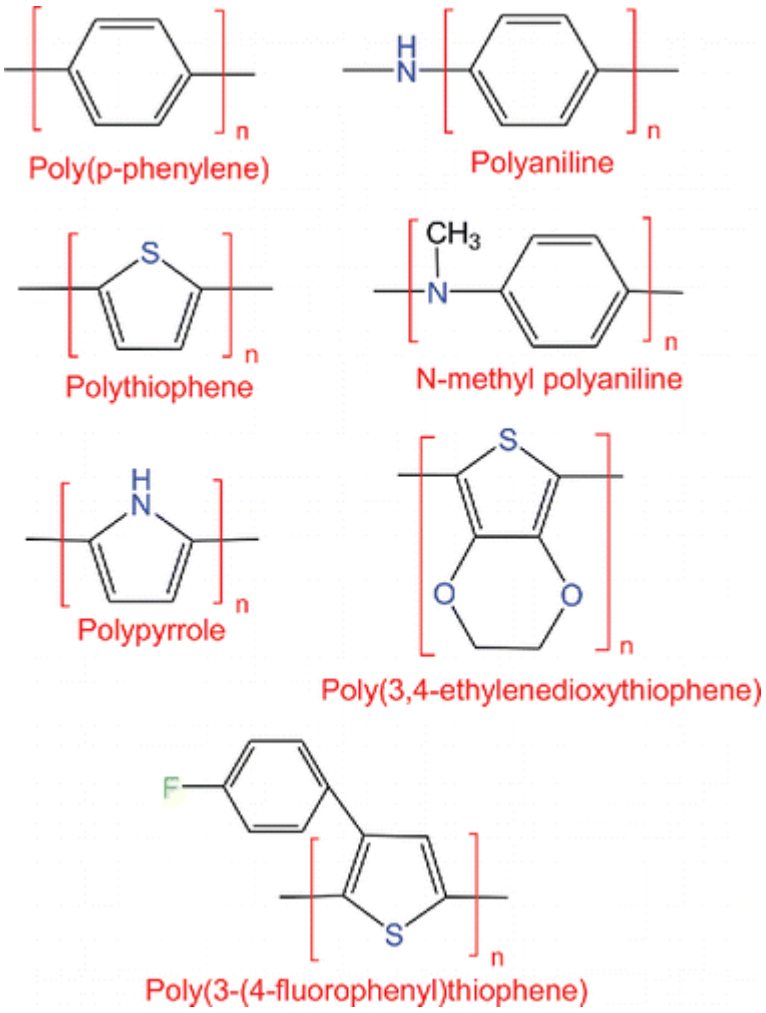

Figure 5. Molecular structures of representative conducting polymers [31].

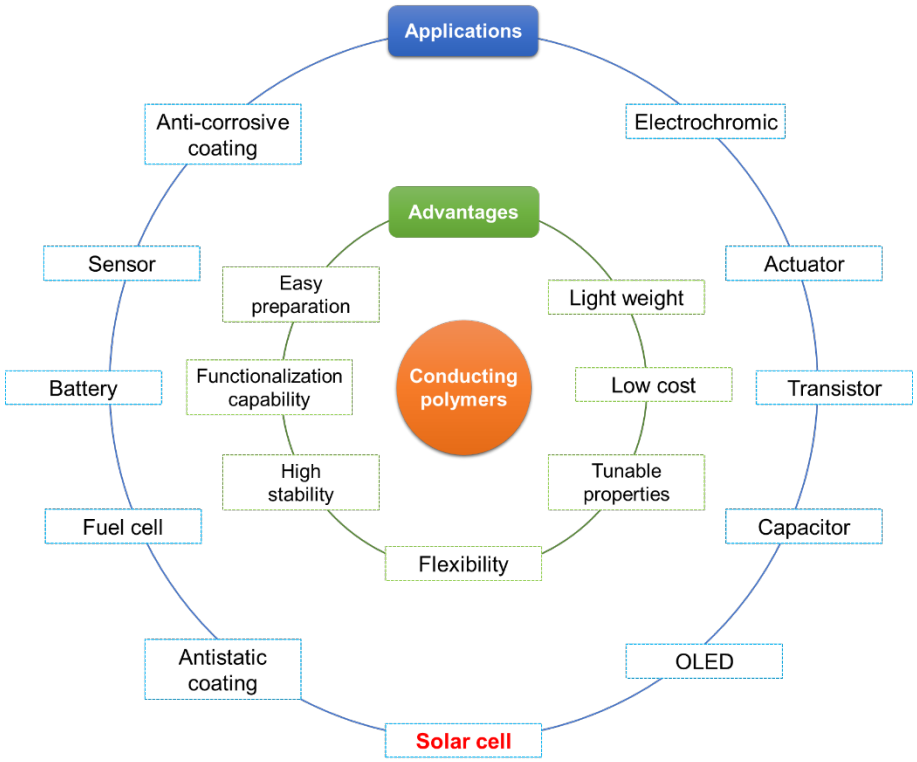

Figure 6. Advantages and applications of conducting polymers.

1.1.2.1. Solution-processable conducting polymers in perovskite solar cells

Charge transport materials including electron transport material (ETM) and HTM have a great influence on efficiency and stability of PSCs. Organic small molecules and metal oxides are commonly employed as charge transport materials. However, solution-processed organic small molecule film is non-uniform and cannot guarantee full coverage [32]. On the other hand, metal oxides limit the potential for tandem and flexible devices owing to their inherent brittleness and the requirement of high-temperature sintering process [33]. Therefore, solution-processable conducting polymers have been intensively investigated as a promising charge transport material because they produce uniform, stable films by simple, inexpensive, and low-temperature process. Using conducting polymers is compatible with the fabrication of low-cost, large-area, flexbile perovskite optoelectronics (**Figure 7**).

Since most conducting polymers are synthesized by chemical oxidative polymerization using an oxidizing agent and dopant (p-type), they have been used as an HTM in PSCs [34]. So far, conducting polymers such as PEDOT:PSS, PTAA, poly(3-hexylthiophene-2,5-diyl) (P3HT), poly(2-methoxy-5-(2-ethylhexyloxy)-1,4-phenylenevinylene)

(MEH-PPV), etc. have been used for an HTM [33]. Among them, the most widely used and commercially available one is PEDOT:PSS since it is solution-processable, highly transparent, highly conductive, and mechanically flexible. However, its hygroscopic and acidic nature induce degradation of the adjacent perovskite layer, which is vulnerable to moisture, and seriously deteriorate device efficiency and stability [35]. In addition, water-dispersed PEDOT:PSS has a limitation that it can be employed only as HTL of inverted PSC structure, which is deposited prior to perovskite layer. PEDOT:PSS and other polymeric HTMs are relatively expensive so they can increase the overall device cost of PSCs. Therefore, it is imperative to develop a stable, versatile, and low-cost conducting polymer HTM.

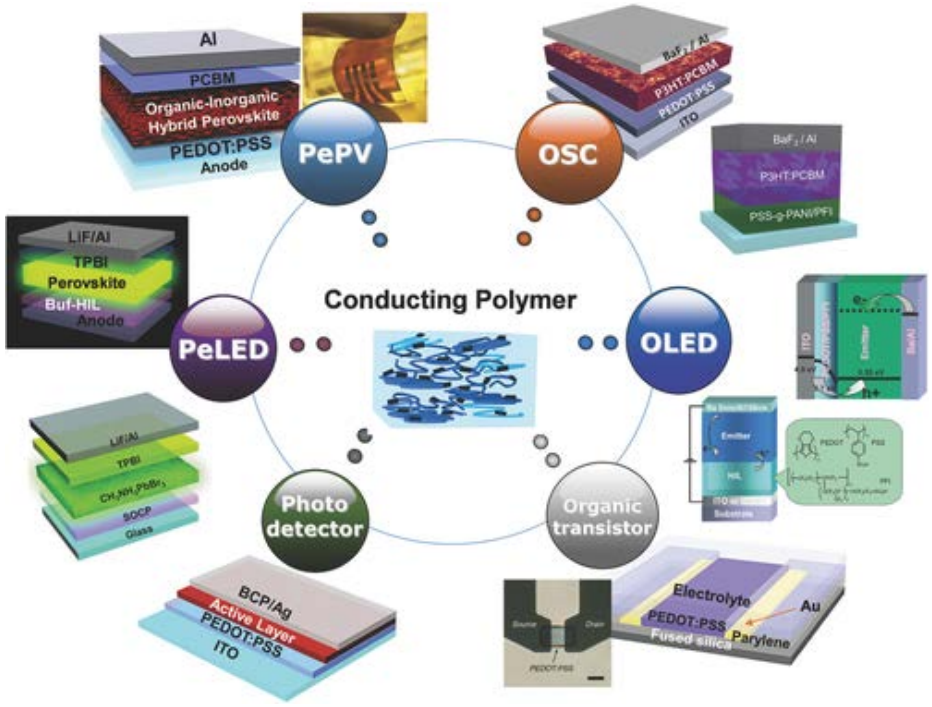

Figure 7. Applications of solution-processable conducting polymers to optoelectronics [28].

1.1.2.2. Polyaniline

Since the first report on conducting polyaniline (PANI) by MacDiarmid and co-workers, PANI have attracted tremendous interest due to its unique redox and doping/dedoping properties, good conductivity, excellent environmental stability, and especially low cost of the starting material [36]. Aniline, the starting material of PANI, is the least expensive among all the conducting polymers because it is readily produced from benzene or extracted as a by-product from oil and coal tar refining [37]. However, despite these advantages, there are only few studies which employ PANI in PSCs, and the associated devices showed poor photovoltaic parameters or required complex, unreproducible fabrication procedures [38-40].

Generally, polyaniline has three major oxidation states as shown in **Figure 8a**: Leucoemeraldine (fully reduced), emeraldine (half-oxidized), and pernigraniline (fully oxidized). The most useful structure is electrically conductive emeraldine. As illustrated in **Figure 8b**, insulating emeraldine base (EB) can be converted to conductive emeraldine salt (ES) by protonation of acid, which is known as doping [34]. PANI ES, which is the most stable oxidation states, is usually obtained by chemical oxidative polymerization as described in this

dissertation.

Two types of solution-processable polyaniline are prepared and utilized as an HTL of PSCs in this dissertation: polyaniline:poly(styrenesulfonate) (PANI:PSS) and polyaniline doped with camphorsulfonic acid (PANI-CSA) (**Figure 9**).

PANI:PSS is synthesized by polymerization of aniline where the monomers electrostatically interact with sulfonate groups of PSS. In PANI:PSS, polymeric acid PSS is bound to the conducting polymer chains and makes it to be dispersed in water. PSS acts as both charge-compensating counter-ion and water-soluble binder for the conducting polymer. Therefore, water-dispersible PANI:PSS have attracted much attention as an alternative material for PEDOT:PSS. Due to its low cost, simple synthesis, and different colors with oxidation states, PANI:PSS has been used in chemical/bio sensors, electrochromic devices, and optoeletronic devices.

Re-doping PANI with organic protonic acids is an effective strategy to further increase the conductivity. Firstly, primary dopant of the obtained PANI ES can be removed by base dedoping (deprotonation) using ammonia or hydrazine. Deprotonated PANI EB is re-doped using a favorable dopant such as camphorsulfonic acid (CSA) and

dodecylbenzene sulfonic acid (DBSA). Doping with these functionalized organic acids, polyaniline can be dispersible in a number of commonly used organic solvents [41]. Thus, re-doped PANI can produce conductive film by solution process. In particular, PANI-CSA has been mainly used because solution-processed PANI-CSA from m-cresol shows two or three orders of magnitude higher conductivity than that of PANI doped with hydrochloric acid [42]. m-cresol, a good solvent for PANI-CSA, acts as a secondary dopant which contributes to the high conductivity. Interactions between the polar polymer backbone and polar m-cresol induce the conformation change of the polymer backbone from a compact coil structure to expanded structure [43]. The more expanded structure of the polymer backbones promotes compact interchain packing of PANI, leading to increase of electrical conductivity. Due to its high conductivity and good processability from the viscous solvent, PANI-CSA has been employed as charge transport materials in organic light emitting diodes (OLEDs), organic photovoltaics (OPVs), and dye-sensitized solar cells (DSSCs), but not yet in PSCs.

a)

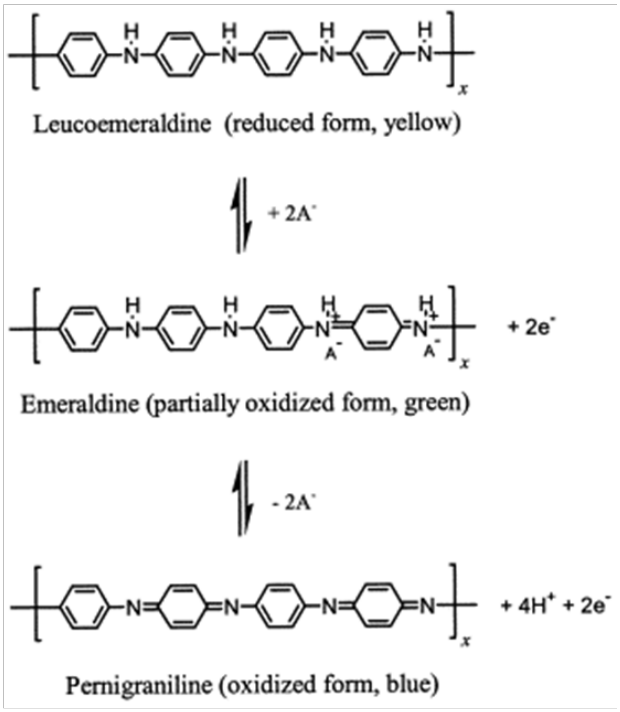

b)

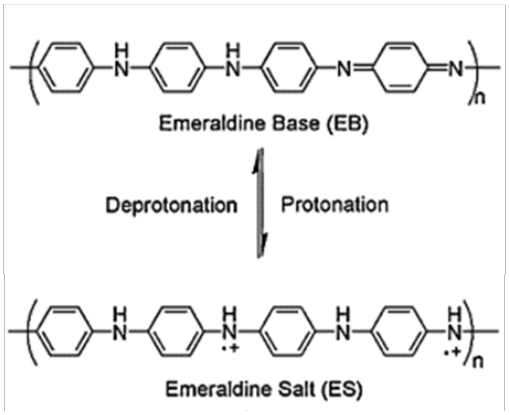

Figure 8. (a) Three predominant oxidation states of PANI [44]. (b) Transition of PANI between EB and ES forms [45].

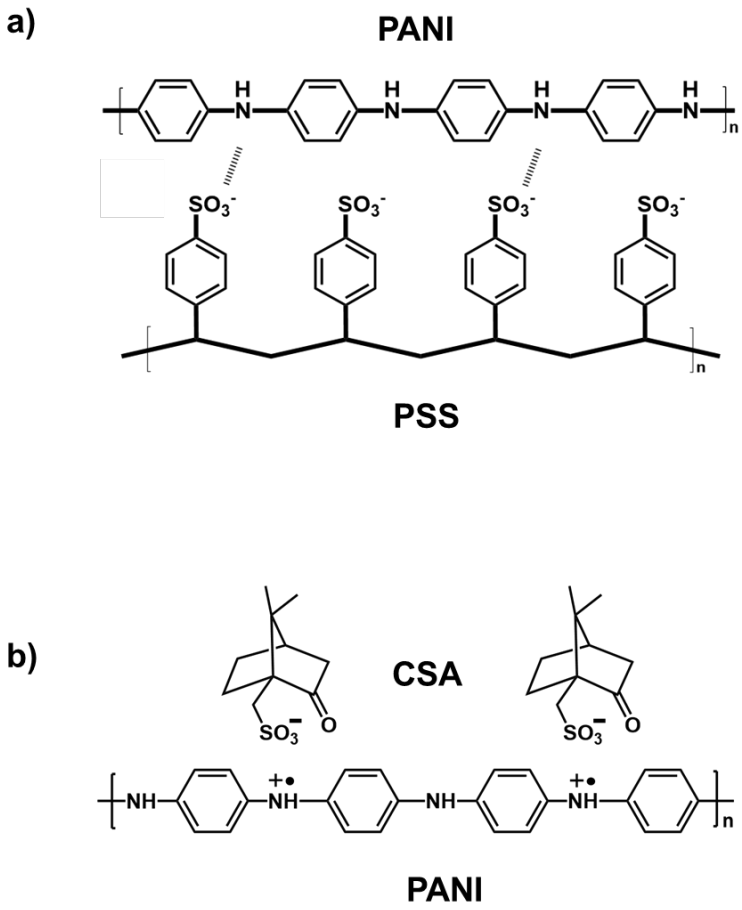

Figure 9. Molecular structures of (a) PANI:PSS and (b) PANI-CSA

1.2. Objectives and Outlines

1.2.1. Objectives

The aim of this dissertation is to describe the methods for application of solution-processable polyaniline to an HTL in various PSC structures. In detail, PANI:PSS and PANI-CSA dispersion solution are synthesized by simple chemical oxidative polymerization, and optimized to obtain improved hole transport ability. This study provide an effective strategy to prepare polyaniline-based HTMs for low-cost, efficient, moisture- and thermal-stable, and flexible PSCs. Furthermore, origins of hole transport ability of solution-processable polyaniline are studied both theoretically and experimentally.

1.2.2. Outlines

This dissertation focused on the fabrication of polyaniline-based HTMs and investigation of their hole transport ability as an HTL in PSCs. This dissertation involves the following subtopics:

I. Surfactant-modified PANI:PSS for HTL of inverted PSCs

II. PANI-CSA for HTL of inverted PSCs

III. PANI-CSA for HTL of carbon electrode-based PSCs

A detailed outline of the study is as follows:

1. Facile synthesis and modification methods of PANI:PSS is described to prepare an efficient HTM in inverted PSCs. PANI:PSS aqueous dispersion solution is prepared via chemical oxidative polymerization of aniline in the presence of PSS. Triton X–100, a nonionic surfactant, is added to the PANI:PSS dispersion to enhance hole transport ability. The surfactant lowered the surface tension of a PANI:PSS aqueous solution, which enabled uniform casting of PANI:PSS films onto an substrate without any surface treatment. Additionally, self-organization of PSS nanogranules, induced by the surfactant, provided PANI-rich surfaces that were favorable for hole extraction. Due to improved wetting on the substrate and a surface compositional change, the average J_{SC} increased by 23% compared with pristine PANI:PSS (i.e., from 15.02 to 18.43 mA cm^{-2}) and the fill factor also improved, eventually leading to a PCE enhancement from 6.59 to 10.90%.

2. PANI-CSA is introduced as an HTL in inverted PSCs and its hole transport ability is examined in comparison with PEDOT:PSS, the

most commonly used HTM. PANI-CSA can produce a highly conductive film due to expansion of chain conformation by m-cresol, which is an effective secondary dopant as well as a good solvent. PANI-CSA exhibits higher conductivity and charge mobility than those of PEDOT:PSS in the *I–V* characteristic. Consequently, the device using PANI-CSA exhibited superior photovoltaic performance, with a maximum efficiency of 15.42% (14.11% for the device using PEDOT:PSS). Most notably, the device using PANI-CSA was much more stable than the device using hygroscopic PEDOT:PSS, due to its moisture resistance.

3. PANI-CSA is introduced as an HTL in carbon electrode-based PSCs and effect of HTL insertion is investigated. Carbon electrode-based PSC is an ideal architecture to realize highly stable device under humid and thermal conditions. However, carbon electrode-based devices suffer from severe charge recombination at perovskite/carbon interface because of the absence of HTM. Spiro-OMeTAD is the most commonly used HTM for normal PSC structure, which is deposited on perovskite layer. However, its vulnerability to heat limits the use in carbon electrode-based PSC owing to the following curing process at

above 100 °C. PEDOT:PSS, the other commonly used HTM, is thermally stable but cannot be processed on perovskite layer owing to its water solvent. To resolve this issue, PANI-CSA is employed as an HTL in carbon electrode-based PSCs, which is thermally stable and dispersed in non-polar solvents. Using PANI-CSA HTL, the device efficiency increases from 11.46% to 13.17% and achieves the maximum value of 13.51%. In stability test, the carbon electrode-based PSC with PANI-CSA HTL retains 83% of its initial efficiency over a month of ambient exposure and shows little degradation after heating at 100 °C. These results demonstrate that carbon electrode-based PSC with PANI-CSA HTL is highly stable due to hydrophobic and heat-resistant properties of both PANI-CSA and carbon layers.

2. Experimental Details

2.1. Surfactant-modified PANI:PSS for HTL of inverted PSCs

2.1.1. Synthesis of surfactant modified-PANI:PSS solution

PANI:PSS solution was synthesized by chemical oxidation polymerization of aniline in the presence of HCl and PSS. First, 17 mg of aniline monomer (0.18 mmol) was introduced drop-wise in 0.35 M aqueous HCl solution (11.66 mL) and was stirred for 2 h. Then, 0.4 g of commercially available PSS solution (Mw ~200,000, 30 wt% in water, Sigma Aldrich) was added to the mixed solution followed by vigorous stirring for 2 h. The polymerization was carried out by adding 52 mg of ammonium persulfate (0.23 mmol) as an oxidant over 12 h at 25 °C. As a result of polymerization, dark green solution of PANI:PSS was obtained. Afterwards, PANI:PSS solution was mixed with different weight percentage of Triton X–100 (0.5, 1.0, and 2.0 wt%), and used as a hole transport material of perovskite solar cells without further purification.

2.1.2. Fabrication of PSCs using s-PANI:PSS as HTL

The devices were fabricated on patterned indium tin oxide (ITO) glass with a sheet resistance of 15 Ω sq^{-1} (Pilkington). ITO substrates were cleaned sequentially in deionized (DI) water, acetone, and 2-propanol for 30 min. A PANI:PSS layer was deposited by spin-coating a prepared PANI:PSS solution at 2,000 rpm, and annealed at 125 °C for 10 min in ambient air. Cs-doped $FAPbI_3$ precursor solution was prepared by dissoving 0.159 g of FAI, 0.026 g of CsI, and 0.507 g of PbI_2 in 0.75 mL of dimethylformamide:dimethyl sulfoxide (DMF:DMSO; v/v = 9/1) mixed solvent, and stirred at 70 °C. The perovskite precursor solution was spun-cast on the pre-heated substrate at 1,000 rpm for 10 s and 4,000 rpm for 25 s under a N_2 atmosphere. During the second spin coating step, 0.4 mL of diethyl ether (> 99.5 %) was dropped onto the substrate to promote fast crystallization of perovskite layer. After the whole spin coating process, the substrate was annealed at 125 °C for 10 min in ambient air to form Cs-doped $FAPbI_3$ films (humidity < 40%). The ETL was spin-coated from a PCBM solution (20 mg mL^{-1} in chlorobenzene) at 4,000 rpm for 30 s. Finally, a 60-nm-thick Au top electrode was deposited by thermal evaporation. The active area of the fabricated device was 0.09 cm^2.

2.1.3. Characterization of s-PANI:PSS and the fabricated PSC

FE-SEM images were obtained with JSM-6701F microscopes (JEOL, Japan). XRD of $FAPbI_3$ films was measured using Smartlab (Rigaku, Japan). Transmittance of PANI:PSS films and UV-VIS absorption spectra of the $FAPbI_3$ films were measured with a Lambda 35 (Perkin-Elmer, USA). AFM images of PANI:PSS films were acquired using an Innova SPM (Vecco, USA) and analyzed with SPMLabAnalysis software. The *J–V* characteristics of the PSCs were measured under standard AM 1.5G (100 mW cm^{-1}) illumination from a 500-W xenon lamp. EQE was characterized from 350 nm to 850 nm using a K3100 incident photon-to-current efficiency (IPCE) Measurement System (McScience Inc., Korea; chopping frequency of 4 Hz, without bias light and 10-nm step wavelength). Time-resolved PL decay transients were recorded using a 405 nm pulse laser (PicoQuant). EIS of the PSCs were obtained by Zive Labs (Wonatech, Korea).

2.2. PANI-CSA for HTL of inverted PSCs

2.2.1. Synthesis of PANI-CSA dispersion solution

PANI powder was synthesized using a self-stabilized dispersion polymerization (SSDP) method to reduce undesirable side reactions; with this method, chemical oxidative polymerization occurs at the aqueous medium/organic solvent interface at low temperatures. 2 g of aniline monomer was added to 40 mL of 1.2 M HCl aqueous solution. Then, 60 mL of chloroform was poured into the aqueous anilinium ion solution to induce interfacial polymerization of aniline monomers. Oxidizing agent was prepared by dissolving 2.4 g of ammonium persulfate in 15 mL of 2 M HCl aqueous solution. The resulting oxidizing agent was added into the reaction medium to initiate polymerization. The polymerization of aniline proceeded with vigorous stirring for 16 h at –40 °C. After washing with water, ethanol, and acetone, precipitates of greenish PANI ES powder were obtained. The PANI ES powder was dispersed in 200 mL of 0.6 M NH_4OH aqueous solution and stirred for 12 h to fully reduce. The products were washed with water, ethanol, and acetone to produce brownish PANI EB powder. Re-doping of the PANI EB powder was conducted by grinding with CSA (the mole ratio of CSA to aniline = 1:2) using a mortar. CSA-doped PANI powders were dispersed in m-cresol/chloroform (v/v = 7/3) co-solvent to a concentration of 3 mg

mL^{-1}. The PANI-CSA dispersion was vigorously stirred and sonochemically treated for 24 h to obtain homogenous dispersion. Before use, the dispersion was diluted to 0.5 mg mL^{-1} by adding chloroform.

2.2.2. Fabrication of PSCs using PANI-CSA as HTL

The PSCs were fabricated on patterned, FTO-coated glass with a sheet resistance of 15 Ω sq^{-1}. FTO substrates were cleaned sequentially in DI water, acetone, and 2-propanol for 30 min using an ultra-sonication bath. HTLs were deposited by spin-coating PEDOT:PSS (for control device) and PANI-CSA dispersions at 5,000 rpm and annealing at 120 °C for 20 min. The mixed perovskite ($Cs_{0.05}MA_{0.16}FA_{0.79}Pb(I_{0.84}Br_{0.16})_3$) precursor solution was prepared by dissolving FAI (1 M), PbI_2 (1.1 M), $PbBr_2$ (0.2 M), MABr (0.2 M), and CsI (0.06 M) in DMF:DMSO (v/v = 4/1) co-solvent, with stirring at 60 °C. The perovskite precursor solution was dropped onto the pre-heated substrate at 40 °C, and spin-coated at 1,000 rpm for 10 s and 5,000 rpm for 23 s. After ~15 s of second spin-coating step, 0.3 mL of chlorobenzene was dripped onto the center of the substrate to induce fast crystallization of the perovskite film. After the whole spin-coating

process, the substrate was annealed at 100 °C for 20 min. PCBM solution (20 mg mL^{-1} in chlorobenzene) with Triton X-100 (3 wt% of PCBM) was prepared and deposited *via* spin-coating at 2,500 rpm for 40 s. Finally, a 65-nm-thick Au top electrode was deposited by thermal evaporation. All solar cell fabrication procedures were carried out in ambient air (temperature = 23 °C, relative humidity < 30%).

For the flexible PSCs, PET/ITO substrates were mounted on glass during the fabrication; the fabrication procedures were the same as those described above for the rigid devices.

2.2.3. Characterization of PANI-CSA and the fabricated PSC

The FE-SEM images were obtained from JSM-7800F Prime microscopes (JEOL, Japan). The transmittance of the conducting polymer films and UV–VIS absorption spectra of the perovskite films were measured with a Lambda 35 double beam UV–VIS spectrophotometer (Perkin-Elmer, USA). The UPS spectra were measured by Axis Supra (Kratos, UK) with a minimum step size of 1 meV and sensitivity of 1,000,000 cps at 120 meV resolution. XRD of the perovskite films was measured using SmartLab (Rigaku, Japan). The *J–V* characteristics of the PSCs were measured using an I–V

tracer (MP-160; Eko Instruments, Japan) under standard AM 1.5 G (100 mW cm^{-2}) illumination from a 500 W xenon lamp, calibrated with a KG5-filtered Si reference cell (K801; McScience Inc., Korea). Steady-state photocurrent output and EIS of the PSCs, and *J*–*V* plots of the hole-only devices were measured by the Zive Lab equipment (WonATech, Korea). The Mott-Gurney law equation ($J = (9/8)\mu\varepsilon_0\varepsilon(V^2/d^3)$) was used to determine the charge mobility, where μ, ε_0, ε, and *d* are the charge mobility, free space permittivity, relative dielectric constant, and film thickness, respectively. The relative dielectric constant for both PEDOT:PSS and PANI-CSA is assumed to be 3, which is a typical value for conjugated polymers. The time-resolved PL were measured under exposure to a 520 nm pulse laser (PicoQuant, Germany).

2.3. PANI-CSA for HTL of carbon electrode-based PSCs

2.3.1. Synthesis of PANI-CSA dispersion solution

CSA-doped PANI powders were prepared in the same manners of previous section but dispersed in m-cresol/chlorobenzene (v/v = 7/3) co-solvent to a concentration of 1 mg mL^{-1}. The PANI-CSA dispersion was vigorously stirred and sonochemically treated for 24 h to obtain

homogenous dispersion. Before use, the dispersion was diluted to 0.25 mg mL^{-1} by adding chlorobenzene.

2.3.2. Fabrication of carbon electrode-based PSCs with PANI-CSA HTL

FTO glass substrates were etched with 2 M HCl and Zn powder to form the electrode patterns. The patterned FTO substrates were ultrasonically cleaned in DI water, acetone and isopropyl alcohol for 30 min, sequentially. To deposit a dense TiO_2 compact layer as a hole-blocking layer, a mildly acidic solution of titanium (IV) isopropoxide in ethanol was spin-coated onto the substrate at 3,000 rpm for 30 s and heated at 150 ℃ for 10 min in ambient air. The compact TiO_2 layer coated substrate was then sintered at 500 ℃ for 30 min in muffle furnace. After cooling to the room temperature, a mesoporous TiO_2, which was prepared by diluting TiO_2 paste in ethanol (1: 3.5 at a weight ratio), was spin-coated on the compact TiO_2 layer at 3,000 rpm for 30 s. The substrate was annealed at 150 °C for 10 min and sintered at 500 °C for 60 min. To obtain Li-doped TiO_2, Li-TFSI solution (15 mg ml^{-1} in acetonitrile) was treated on the mesoporous TiO_2 layer by spin-coating at 3000 rpm for 30 s. The treated substrate was heated at

150 ℃ for 10 min, followed by sintering at 500 ℃ for 30 min. The mixed perovskite ($Cs_{0.05}MA_{0.16}FA_{0.79}Pb(I_{0.84}Br_{0.16})_3$) precursor solution was prepared by mixing the FAI (1 M), PbI_2 (1.1 M), $PbBr_2$ (0.2 M), MABr (0.2 M), and CsI (0.06 M) in a mixed solvent of DMF:DMSO (v/v = 4/1). The prepared solution was stirred at 60 °C for 2 h and filtered with 0.45 μm PTFE syringe filter before use. The perovskite precursor solution was cast onto the substrate and spin-coated by two steps at 1,000 and 5,000 rpm for 10 and 23 s, respectively. During the second step, 180 μl of chlorobenzene was dropped on the spinning substrate at 10 s prior to the completion of the process. After the entire spin-coating process, the substrate was immediately placed on 100 °C hotplate and annealed for 45 min to crystallize the perovskite. The as-prepared PANI-CSA dispersion solution was spin-coated onto the perovskite film at 3,000 rpm and annealed at 100 ℃ for 10 min. To deposit a carbon electrode, the carbon conductive paste (FTU-16, Asahi Chemical Research Laboratory) mixed with carbon black (2 wt%) and chlorobenzene was screen-printed on the perovskite layer and cured at 100 °C for 10 min. This depositing procedure was conducted for three times successively. All fabrication processes were conducted under the controlled ambient condition with 25 ℃ and 30% relative humidity.

2.3.3. Characterization of PANI-CSA and the fabricated carbon electrode-based PSC

FE-SEM images of surface morphology and cross section of the device were obtained from JSM-6701F (JEOL Ltd). EDX images and elemental analysis were also obtained from JSM-6701F (JEOL Ltd). Time-resolved PL decay profiles were measured under exposure to 405 nm pulse laser (PicoQuant). The *J–V* characteristics of the PSCs were measured using an I–V tracer (MP-160; Eko Instruments) under standard AM 1.5 G (100 mW cm^{-2}) illumination from a 500 W xenon lamp, calibrated with a KG5-filtered Si reference cell (K801; McScience Inc). The IPCE spectra were characterized using K3100 Solar Cell IPCE System (McScience Inc) without bias light. Stabilized power output, V_{OC} and EIS of the PSCs I–V characteristic of carbon electrode were measured by the Zive Lab equipment (WonATech). EIS spectra were fitted by an equivalent electrical circuit using the Z-view analyst software (ZMAN).

3. Results and Discussions

3.1. Surfactant-modified PANI:PSS for HTL of inverted PSCs

3.1.1. Synthesis of s-PANI:PSS and fabrication of PSCs

Figure 10a depicts the device structure of a PSC fabricated in this section and the molecular structures of PANI, PSS, and Triton X–100. Digital photographs of spin-coated surfactant-modified PANI:PSS (s-PANI:PSS) films on ITO and the fabricated PSC are shown in **Figure 11**. For the preparation of PANI:PSS, aniline monomer protonated by hydrochloric acid was mixed with commercially available PSS (Mw: ca. 200,000) in DI water, and then ammonium persulfate was added to produce free radicals that initiated polymerization. As polymerization proceeded, the colorless reaction mixture slowly turned dark green. An aniline:PSS feed ratio was 1:6 to simultaneously maintain the conductivity and dispersion stability. The synthesized polymer solution did not precipitate due to a strong electrostatic attraction between positively charged PANI and negatively charged PSS. Consequently, the PANI:PSS remained well-dispersed in an aqueous solution for months without agitation.

After completion of the polymerization reaction, Triton X–100

nonionic surfactant was added and the solution was stirred for 1 h. Triton X–100 has an amphiphilic structure with polyethylene oxide functional groups (**Figure 10a**) that causes phase separation of the conducting polymer and PSS [46,47]. To understand the effect of the surfactant on the hole transport ability of PANI:PSS, s-PANI:PSS with different weight percentages of Triton X–100 (0.5, 1.0, and 2.0 wt%) were prepared and used as an HTL in PSCs. All component layers of the s-PANI:PSS-based PSC were spin-coated, except for the top Au electrode. Cesium-doped formamidinium lead iodide ($FAPbI_3$) was selected as the light absorber due to its excellent light absorbing capability and high photo- and moisture stability [48].

Figure 10b shows the energy diagram of the fabricated device. The lowest unoccupied molecular orbital (LUMO) and highest occupied molecular orbital (HOMO) levels of the s-PANI:PSS film were determined using cyclic voltammetry (CV) in **Figure 12**. The LUMO and HOMO levels of s-PANI:PSS were calculated using the following equations:

$$E_{LUMO} = -e(E_{reduction} + 4.4)\ (eV)$$

$$E_{HOMO} = -e(E_{oxidation} + 4.4)\ (eV),$$

where $E_{reduction}$ and $E_{oxidation}$ are the onset of the reduction and oxidation

currents, respectively [49]. Based on the reduction/oxidation potentials from the CV data, the LUMO and HOMO levels were estimated to be −3.7 and −4.9 eV, respectively. The HOMO level of s-PANI:PSS (−4.9 eV) is well-matched with the valence band of the perovskite layer (−5.4 eV), and hence facilitates efficient hole extraction. Inversely, the higher LUMO level of s-PANI:PSS (−3.7 eV) than the conduction band of the perovskite layer (−4.0 eV) prevents unwanted electron transfer from the perovskite layer to the ITO electrode.

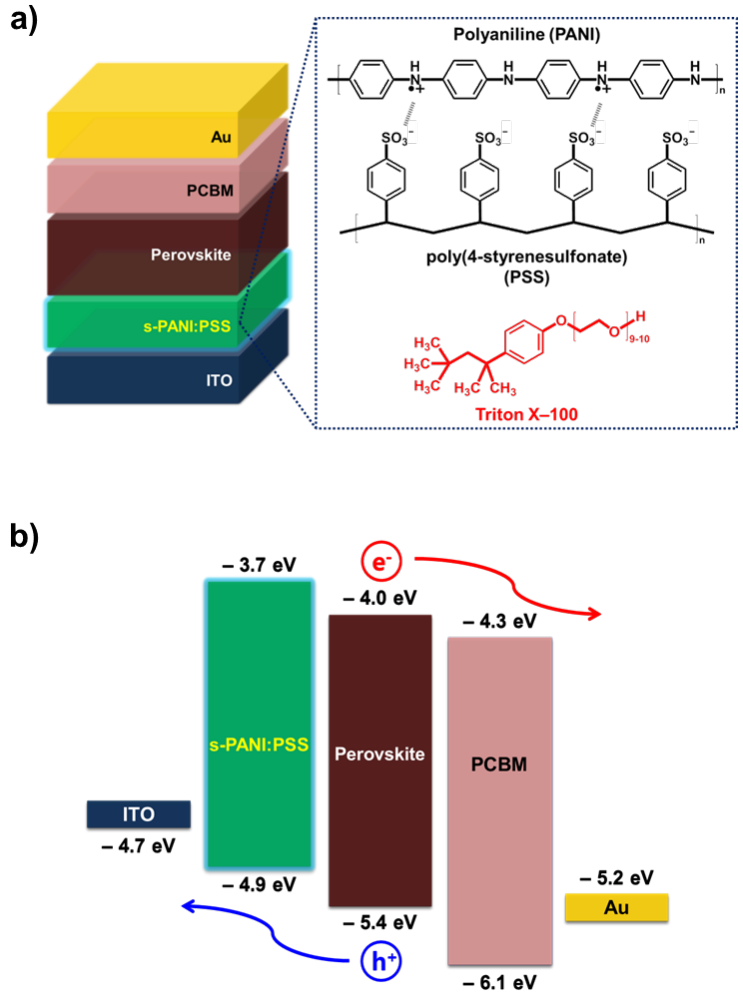

Figure 10. (a) Schematic illustration of the PSC configuration, of which the hole transport layer is s-PANI:PSS. The molecular structures of PANI, PSS, and Triton X–100 are shown. (b) Energy band diagram of the components in the PSC showing ideal electron and hole transport processes. The energy levels of perovskite and PCBM were derived from references [50] and [51].

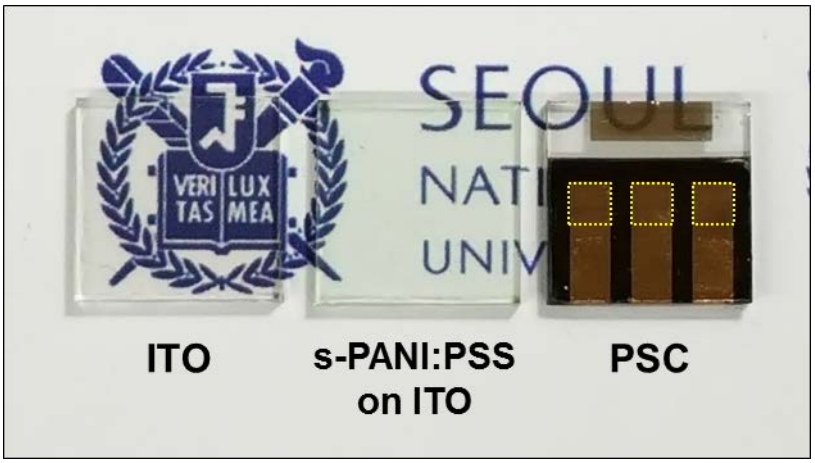

Figure 11. Digital photograph of bare ITO glass, s-PANI:PSS-coated ITO/glass, and the fabricated PSC. The dashed yellow squares on the PSC represent active areas of the cell (0.09 cm^2).

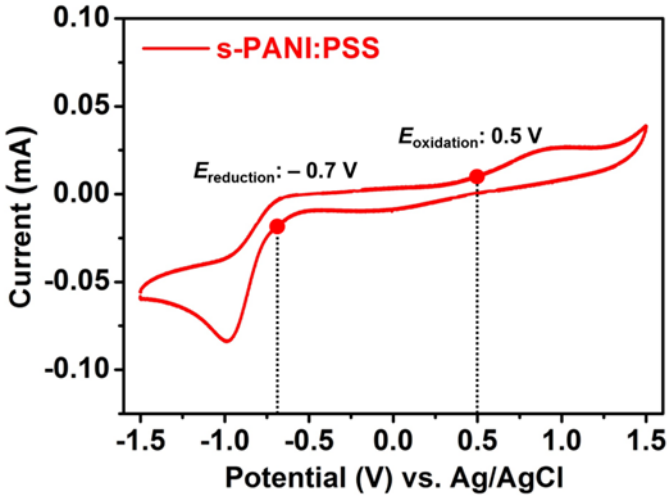

Figure 12. CV curve for s-PANI:PSS at a 100 mV s^{-1} scan rate in 0.1 M solution of tetrabutylammonium hexafluorophosphate ($TBAPF_6$) in acetonitrile. CV measurements were carried out using the standard three-electrode system. Glassy carbon disk, platinum wire, and Ag/AgCl were used as the working, counter- and reference electrodes, respectively. The sample was prepared by drop-casting a s-PANI:PSS solution onto the glassy carbon disk.

3.1.2. Photovoltaic performance of the fabricated PSCs

The *J–V* characteristics of the device using PANI:PSS with varied surfactant concentrations are displayed in **Figure 13**, and the photovoltaic parameters are listed in **Table 1**. The photovoltaic performance of the PANI:PSS-based PSC was clearly influenced by the addition of Triton X–100. Noticeable improvements were observed in the short-circuit current density (J_{SC}), open-circuit voltage (V_{OC}), and fill factor (FF), which led to a significant increase in the average PCE from 6.59 to 10.90%. The optimized amount of Triton X–100 was determined to be 1.0 wt% of the PANI:PSS solution; higher surfactant concentrations reduced the cell efficiency due to the insulating nature of Triton X–100. The optimal device yielded the maximum PCE of 11.67%, a J_{SC} of 18.89 mA/cm^2, an V_{OC} of 0.87 V, and a FF of 0.71. The J_{SC} values of the PSCs using s-PANI:PSS were in good agreement with the external quantum efficiency (EQE) spectra shown in **Figure 14**. In particular, the EQE spectrum of the device using s-PANI:PSS with 1.0 wt% Triton X–100 exhibited a broad plateau at ca. 73% over the range of 400–800 nm. **Figure 15** illustrates the efficiency distribution that was affected by the presence of surfactant in the PANI:PSS. Surfactant addition to the PANI:PSS

not only increased the cell efficiency but also resulted in a narrower efficiency distribution, which indicated better reproducibility. Additionally, the thickness for the s-PANI:PSS (1.0 wt% Triton X–100) layer was optimized. The s-PANI:PSS solution was spin-coated at 2,000, 3,500, and 5,000 rpm, resulting in 130-, 90-, and 50-nm-thick films, respectively (**Figure 16**). The fabricated device with a 130-nm-thick s-PANI:PSS film demonstrated the highest PCE of 11.37% and higher values for J_{SC} and FF.

Hysteresis behavior between forward and reverse scan modes during *J–V* characterization, the so-called *J–V* hysteresis, is an important indicator of cell efficiency and stability. Its origin is not fully understood, but it has been reported that the hysteresis behavior is highly dependent on electron/hole selective contact itself or the interface with the perovskite layer [52]. **Figure 17** compares the *J–V* characteristics of PANI:PSS-based PSCs under forward and reverse scan directions; the related photovoltaic parameters are summarized in **Table 2**. The PCE of the PSC using pristine PANI:PSS decreased from 7.43 to 4.92% in the forward scan mode due to the considerably reduced V_{OC} and *FF*. However, the *J–V* hysteresis of the cell was markedly relieved for s-PANI:PSS and exhibited a relatively small

efficiency loss in the forward scan mode (i.e., from 11.17 to 10.85%). Hysteresis analysis indicated that s-PANI:PSS improved the reliability of the cell efficiency in addition to the photovoltaic performance.

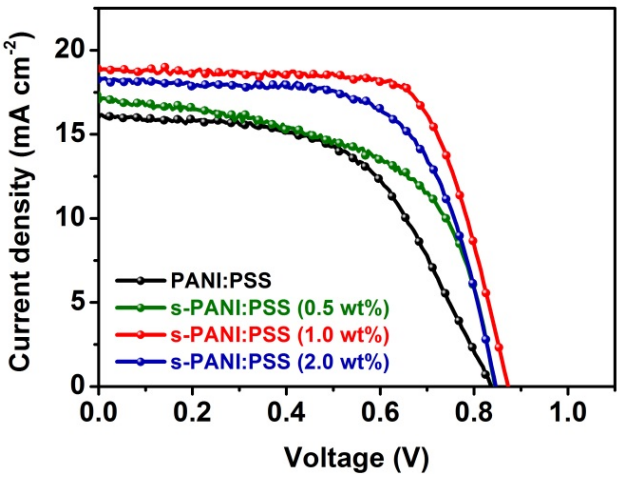

Figure 13. *J–V* curves for the best-performing devices obtained with PANI:PSS and s-PANI:PSS hole transport layers, measured under standard AM 1.5G 100 mW cm^{-2} illumination.

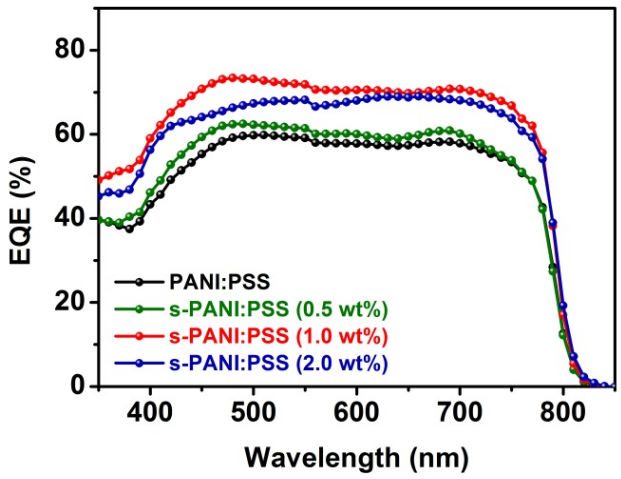

Figure 14. EQE spectra of the PSCs with different PANI:PSS layers.

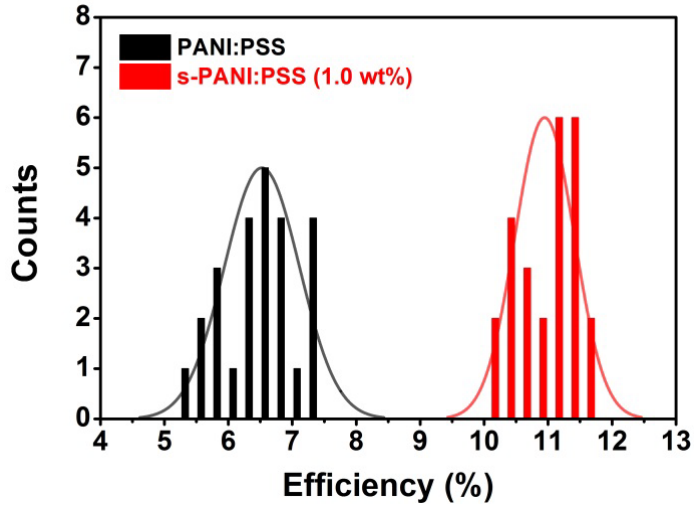

Figure 15. PCE distribution of PSCs with pristine PANI:PSS and s-PANI:PSS (1.0 wt% Triton X–100).

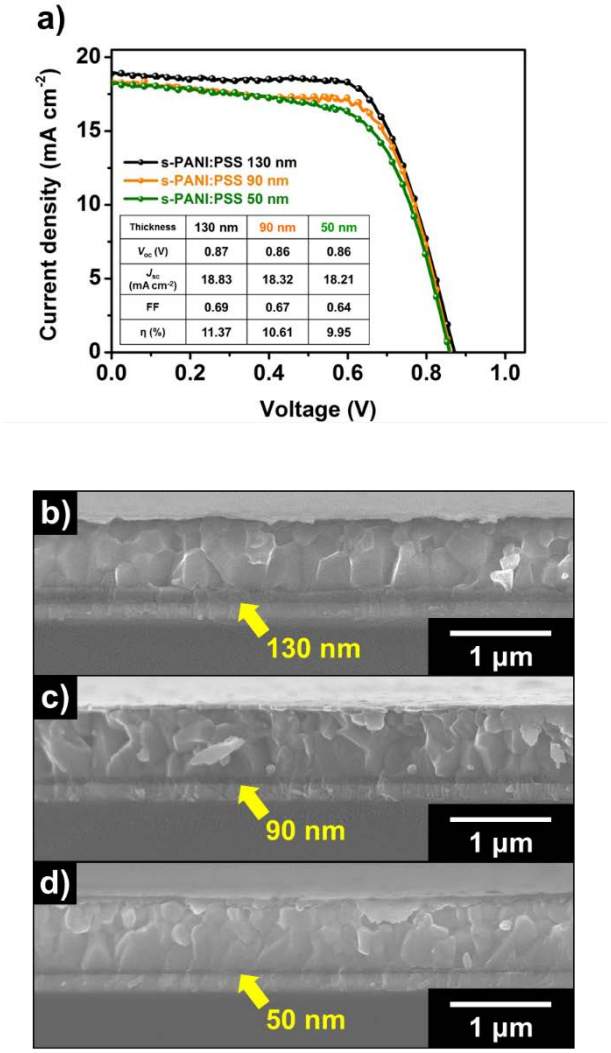

Figure 16. (a) *J–V* curves and (b–d) cross-sectional FE-SEM images of PSCs using s-PANI:PSS with thicknesses of 130, 90, and 50 nm, respectively; the spin-coating rates to prepare the respective s-PANI:PSS layers were 2,000, 3,500 and 5,000 rpm. The surfactant concentration of the s-PANI:PSS solution was 1.0 wt%.

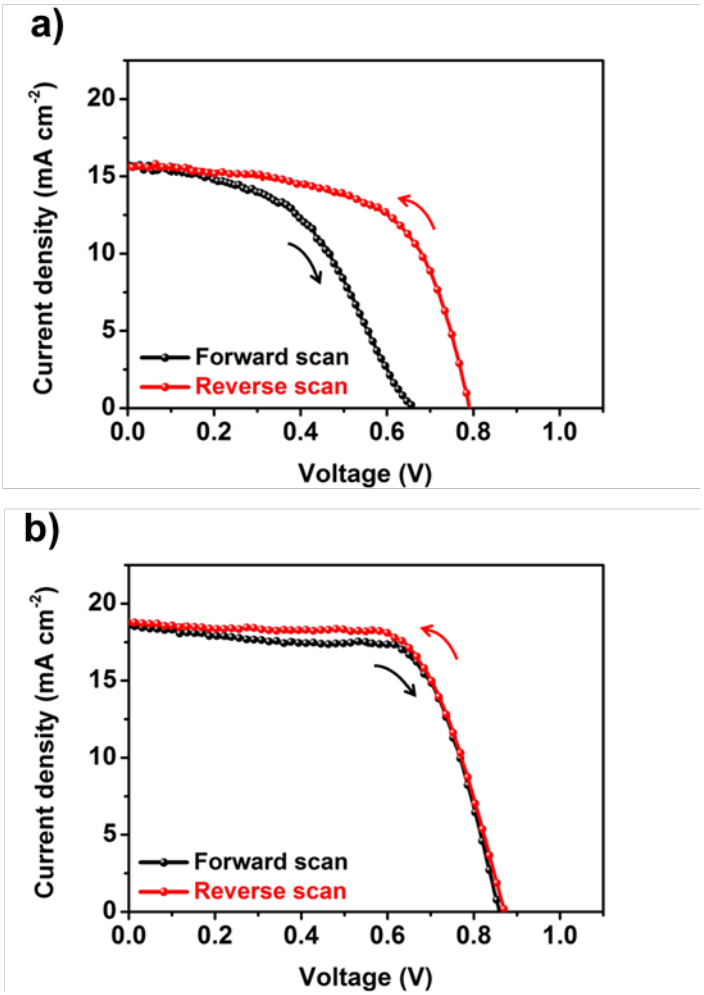

Figure 17. *J–V* curves of PSCs made with (a) PANI:PSS and (b) s-PANI:PSS HTLs depending on the scan direction.

Table 1. Photovoltaic parameters of PSCs using PANI:PSS and s-PANI:PSS HTLs.

HTL	V_{OC}[a] (V)	J_{SC}[a] (mA cm^{-2})	FF[a]	η_{avg}[a] (%)	η_{max} (%)
PANI:PSS	0.77	15.02	0.57	6.59	7.46
s-PANI:PSS (0.5 wt%)	0.80	16.28	0.59	7.67	8.34
s-PANI:PSS (1.0 wt%)	0.85	18.43	0.69	10.90	11.67
s-PANI:PSS (2.0 wt%)	0.81	18.04	0.66	9.63	10.01

[a] Average values of the parameters were obtained for 25 devices.

Table 2. Photovoltaic parameters of PSCs using PANI:PSS and s-PANI:PSS HTLs measured for different scan directions.

HTL	Scan direction	V_{OC} (V)	J_{SC} (mA cm^{-2})	*FF*	η (%)
PANI:PSS	Forward[a]	0.66	15.70	0.47	4.92
	Reverse[a]	0.79	15.69	0.60	7.43
s-PANI:PSS	Forward[a]	0.86	18.55	0.68	10.85
	Reverse[a]	0.87	18.68	0.69	11.17

[a] The scan rate of the forward and reverse scan modes was 0.35 V/s.

3.1.3. Effect of surfactant modification to wetting property and film morphology of PANI:PSS

One effect of surfactant modification using Triton X–100 was to reduce the surface tension of an aqueous PANI:PSS solution; this improved the wetting of PANI:PSS on the ITO substrate. **Figure 18a** displays the surface tension of PANI:PSS solutions with different Triton X–100 concentrations. The pristine PANI:PSS had a high surface tension of 69.2 mN m^{-1}, which is close to that of pure water (71.8 mN m^{-1}) [53]. The addition of 0.5 wt% of Triton X–100 caused a steep drop in the surface tension to below half that of a pristine PANI:PSS solution (i.e., to 31.0 mN m^{-1}). Increasing the surfactant concentration to 1.0 and 2.0 wt% caused the surface tension to decrease slightly (i.e., to 29.8 and 29.5 mN m^{-1}, respectively). **Figure 18b** shows optical microscopy images of PANI:PSS and s-PANI:PSS droplets on an ITO surface. The contact angles of the polymer solutions on ITO displayed the same trend as the surface tension measurements, indicating wettability enhancement. An s-PANI:PSS solution immediately spread on the ITO substrate and provided a continuous film during spin coating. Consequently, a PANI:PSS solution containing the surfactant could be used to form a more

uniform HTL compared with pristine PANI:PSS (**Figure 19**). No additional treatment such as plasma or ultraviolet–ozone (UVO) surface modifications was required. These factors could favorably influence photovoltaic performance and cell efficiency distribution.

In addition to improving the wetting properties of PANI:PSS, Triton X–100 induced a substantial change in the surface morphology and composition of PANI:PSS films and enabled better hole transport from the perovskite layer to the ITO substrate. Previous research reported that Triton X–100 can provoke segregation of PEDOT and PSS domains by phase-separation and cause nanofibril structures of both polymers to form with sharp interfaces [46]. However, the addition of Triton X–100 to PANI:PSS had a completely different effect on the surface morphology than in the PEDOT:PSS system. SEM images (**Figure 20**) show the surface morphologies of PANI:PSS and s-PANI:PSS films according to the surfactant concentration (0.5, 1.0, and 2.0 wt%). The pristine PANI:PSS film was composed of tiny (<10 nm) PANI–PSS complex nanoparticles. Adding 0.5 wt% Triton X–100 caused excess PSS to start building segregated domains on the film surface; self-organized nanogranules about 100-nm in length were fully formed in the presence of more than 1.0 wt% of surfactant.

Atomic force microscopy (AFM) phase images (**Figure 21**), where dark and bright regions correspond to PANI-rich (hard segment) and PSS-rich (soft segment) regions, respectively, confirmed phase separation and the formation of PSS nanogranules on the film surface [54]. The small variation of brightness level (softness) for the pristine PANI:PSS film indicated a homogeneous distribution of PANI and PSS chains (**Figure 21a**). In strong contrast, **Figure 21b** shows separated domains of PSS nanogranules and PANI-rich regions in the s-PANI:PSS film. Self-organization of PSS nanogranules on the film surface was caused by Triton X–100, which revealed PANI-rich regions. Direct contact of these PANI networks with the perovskite layer was beneficial for hole transport process.

A high transmittance of the HTL in the inverted PSC structure is essential for efficient light absorption by the perovskite layer. Despite of the marked change in surface morphology, the s-PANI:PSS-coated ITO substrate maintained a high transmittance of over 80% in the visible and near-infrared regions. Thus, loss of light arising from the morphological change of PANI:PSS was expected to be negligible (**Figure 22**).

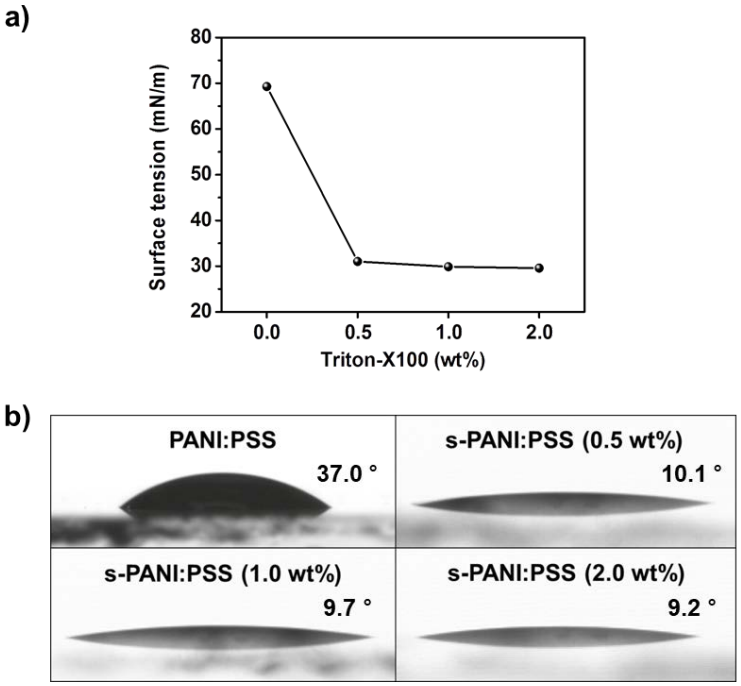

Figure 18. (a) Surface tension of PANI:PSS solutions with different Triton X–100 concentrations. (b) Optical microscopy images and contact angles of PANI:PSS solutions with different Triton X–100 concentrations on ITO substrates.

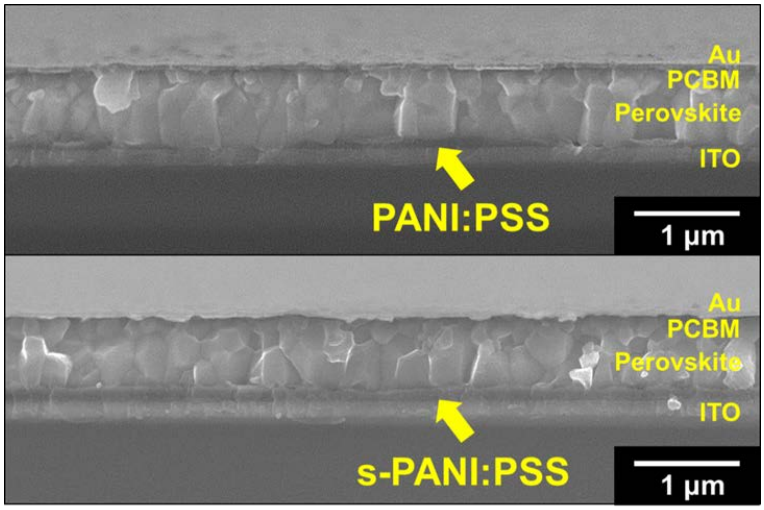

Figure 19. Cross-sectional FE-SEM images of PSCs made with PANI:PSS and s-PANI:PSS. The yellow arrows indicate the PANI:PSS and s-PANI:PSS layers.

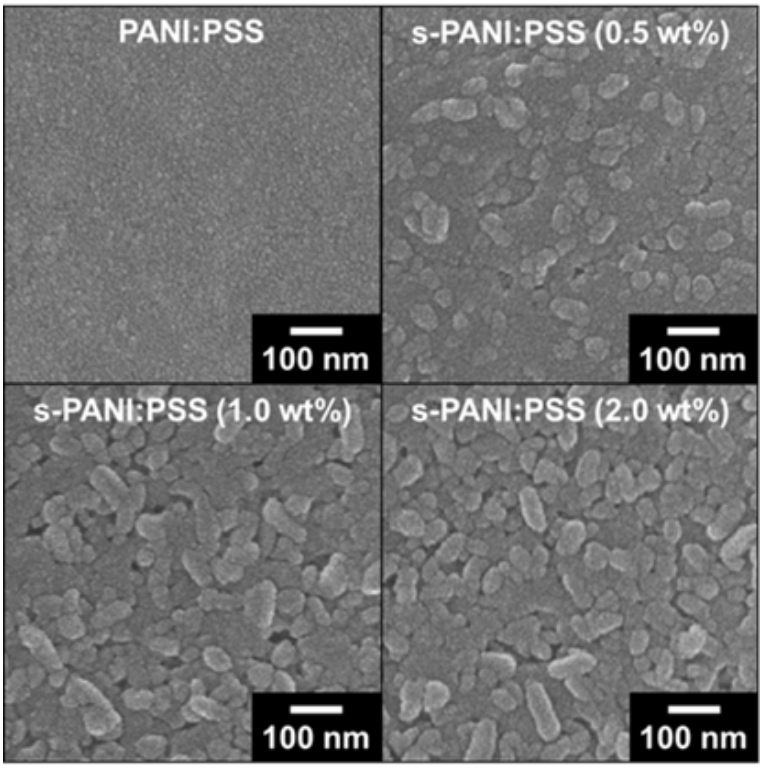

Figure 20. FE-SEM images of spin-coated PANI:PSS and s-PANI:PSS for different Triton X–100 concentrations (0.5, 1.0, and 2.0 wt%).

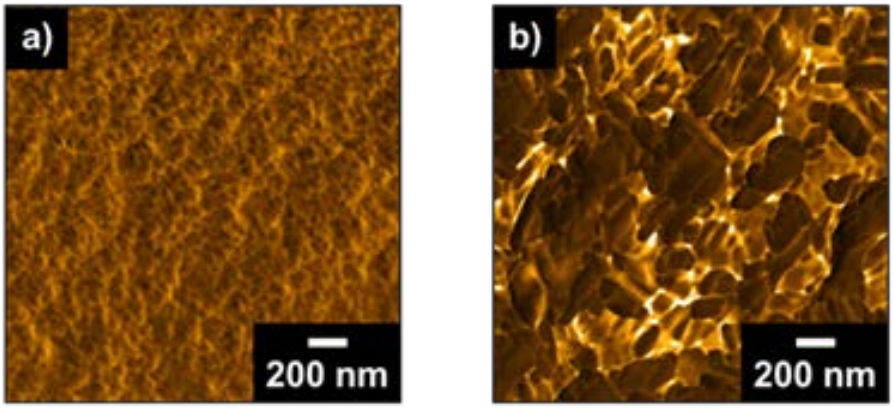

Figure 21. AFM phase images of spin-coated (a) PANI:PSS and (b) s-PANI:PSS (with 1.0 wt% Triton X–100) films.

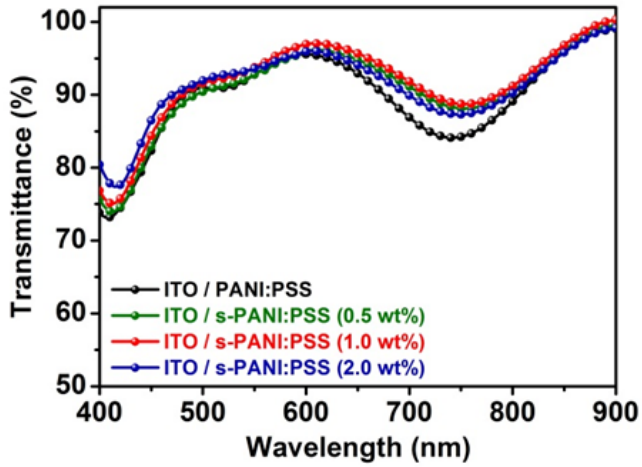

Figure 22. Transmittance spectra of PANI:PSS films with different surfactant concentrations spin-coated on ITO glass.

3.1.4. Effect of surfactant modification to hole transport ability of PANI:PSS

Prior to investigation of hole transport ability of s-PANI:PSS, field emission-scanning electron microscopy (FE-SEM), X-ray diffraction (XRD) and ultraviolet-visible (UV-VIS) absorption measurements were performed to identify the influence of Triton X–100 in PANI:PSS on perovskite morphology, crystallinity, and light absorption. In **Figure 23**, all perovskite films consisting of 200 nm-sized crystallites are thoroughly coated on the substrates and show no difference in their morphology. The XRD patterns (**Figure 24a**) show that all of the perovskite films on PANI:PSS made with the different surfactant concentrations had the same patterns with characteristic peaks corresponding to the black phase of $FAPbI_3$ [48]. The UV-VIS absorption spectra of perovskite films (**Figure 24b**) also remained nearly unchanged by the addition of surfactant to PANI:PSS. These observations indicated that there was no significant change in the structural or optical properties of the perovskite film, and that the improved photovoltaic performance solely originated from efficient hole extraction of s-PANI:PSS.

To quantify the improved hole extraction capability of the s-

PANI:PSS samples, time-resolved photoluminescence (PL) decay times were measured for the glass/no HTM or PANI:PSS or s-PANI:PSS/perovskite configuration (**Figure 25**). PL decay lifetimes (τ_1 and τ_2) were determined by fitting the decay curves with a bi-exponential function; the results are summarized in **Table 3**. The fast decay (τ_1) is considered to originate from charge carrier transport from the perovskite film to the contacting HTMs, while the slow decay (τ_2) stems from radiative recombination of free charge carriers in the perovskite film [55]. All of the samples exhibited similar τ_2 values, but the τ_1 values of PANI:PSS and s-PANI:PSS were shortened to 18.19 and 11.19 ns, respectively, from that of the reference sample (39.85 ns). In particular, s-PANI:PSS displayed a more rapidly decaying curve than the pristine PANI:PSS, which implied that photo-excited holes were effectively transferred from perovskite to s-PANI:PSS [56]. Electrochemical impedance spectroscopy (EIS) was also conducted to characterize the charge transfer behavior of the devices. **Figure 26** shows Nyquist plots measured at bias of 0.8 V under dark condition and the equivalent circuit model for fitting the spectra. The arcs are ascribed to the charge transfer resistance (R_{CT}) and the plot of the device with s-PANI:PSS has a smaller arc than that with pristine

PANI:PSS [57,58]. It indicates a reduced resistance between s-PANI:PSS and perovskite layer due to the synergistic effect of the uniform coating with rapid hole extraction through PANI-rich regions of the s-PANI:PSS [57,58]. The time-resolved PL and EIS observations suggest that Triton X–100 strengthened the hole transport ability of PANI:PSS, reduced contact resistance at the HTL or interfaces of HTL, and led to higher PSC photovoltaic parameter values.

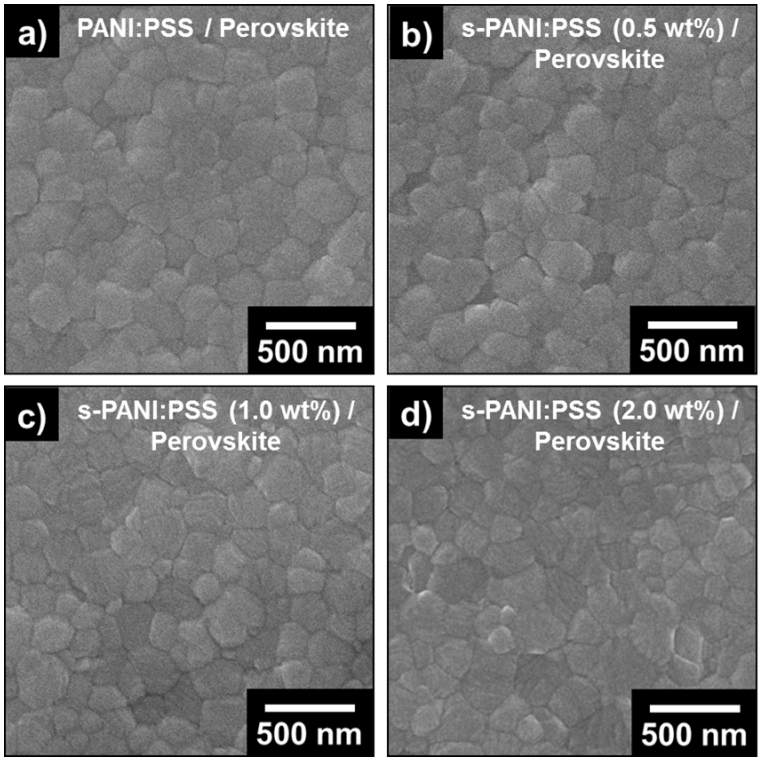

Figure 23. FE-SEM images of perovskite films coated on PANI:PSS with different surfactant concentrations.

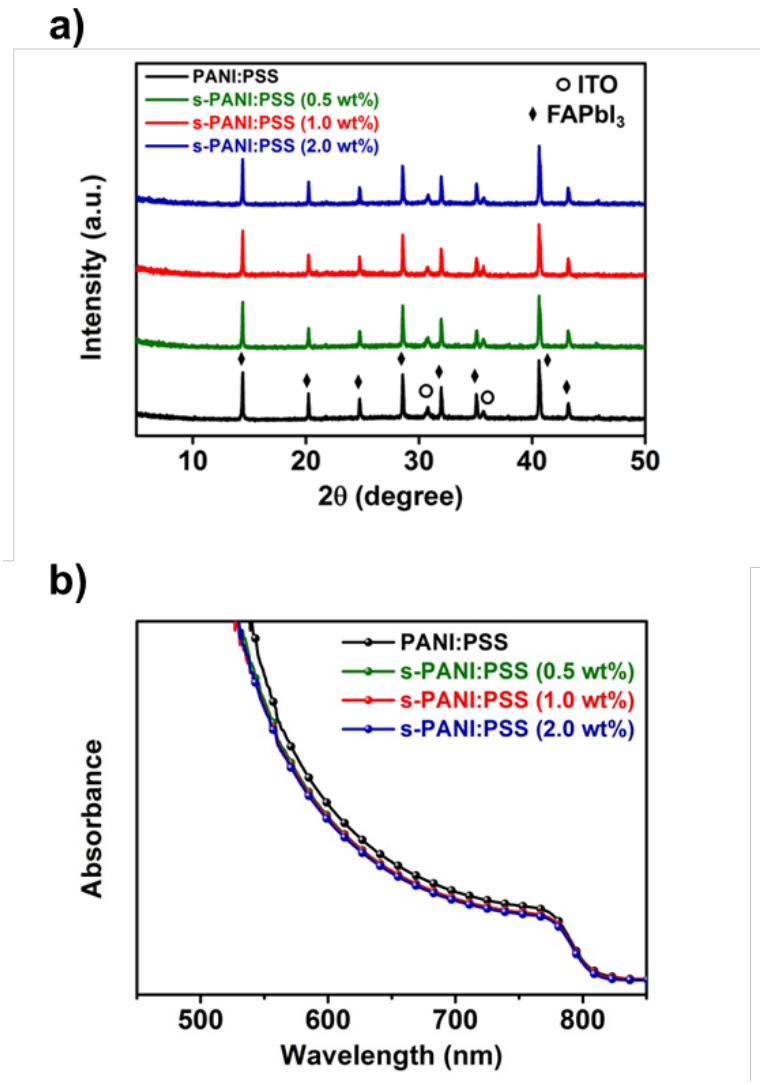

Figure 24. (a) XRD patterns and (b) UV-VIS absorption spectra of perovskite films coated on PANI:PSS with different surfactant concentrations.

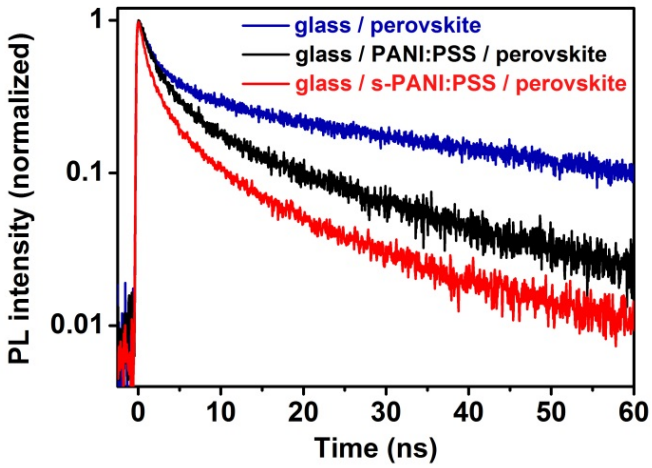

Figure 25. Time-resolved PL decay transients for perovskite films deposited on PANI:PSS and s-PANI:PSS. The samples were excited at 520 nm and PL decay transients were acquired at the peak emission wavelength of 810 nm.

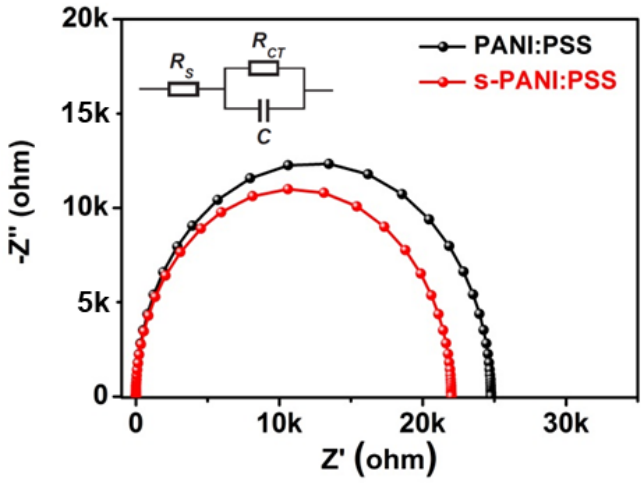

Figure 26. Nyquist plots for the PSCs made with PANI:PSS and s-PANI:PSS measured in the dark at V = 0.8 V. The frequency scan ranged from 0.5 Hz to 3 MHz. The inset is the equivalent circuit.

Table 3. Time-resolved PL decay parameters for perovskite films with PANI:PSS and s-PANI:PSS.

Sample configuration	A_1[a]	τ_1[a]	A_2[a]	τ_2[a]
glass / perovskite	0.32	39.85	0.60	2.15
glass / PANI:PSS / perovskite	0.28	18.19	0.72	2.15
glass / s-PANI:PSS / perovskite	0.25	11.19	0.72	1.35

[a] The bi-exponential fit function is as follows: $y = y_0 + A_1\exp(-t/\tau_1) + A_2\exp(-t/\tau_2)$

3.1.5. Ambient stability of PSCs using s-PANI:PSS HTL

Stability of PSCs based on s-PANI:PSS was tested under ambient condition (temperature ~25 °C, relative humidity ~30%) for 300 h (**Figure 27a**). **Figure 27b** displays *J*−*V* curves of the device before-and-after the 300 h stability test. The J_{SC} was very stable but V_{OC} and FF were decreased, resulting in efficiency degradation from 10.01 to 6.58%. The device efficiency degraded to 65 % of the initial value after 300 h of exposure to the ambient condition due to hygroscopic PSS.

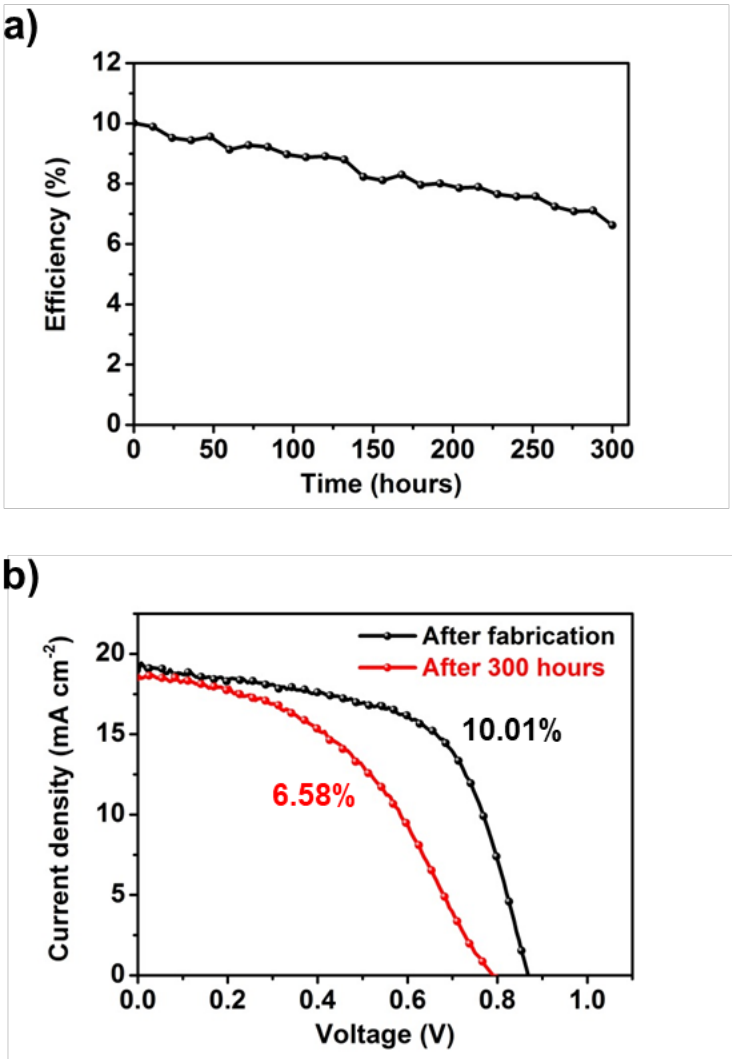

Figure 27. (a) Efficiency of the PSC using s-PANI:PSS upon storage time in ambient air (temperature = 25 °C, relative humidity = 30%) without encapsulation. (b) *J–V* characteristic comparison for the PSC using s-PANI:PSS with storage time of 0 and 300 hrs.

3.2. PANI-CSA for HTL of inverted PSCs

3.2.1. PEDOT:PSS and PANI-CSA HTLs

Figure 28a shows the molecular structure of the conducting polymers used in this section. Conjugated PEDOT is doped with counter-ion PSS to delocalize charge carriers. PSS also acts as a dispersing agent to form a stable aqueous polymer dispersion. PANI transitions from insulating emeraldine base (EB) form to conductive emeraldine salt (ES) form with protonic acid doping. CSA is the preferred substance to protonate PANI because PANI-CSA has good conductivity, two or three orders of magnitude higher than that of PANI doped with hydrochloric acid [59]. PANI-CSA powder is dispersed in m-cresol/chloroform co-solvent. m-cresol acts both as a secondary dopant, to increase conductivity by expanding the polymer chain conformation, and as a viscous solvent to enable a uniform film formation [60,61]. With this method, a highly stable and homogenous PANI-CSA dispersion was obtained with characteristic green color as shown in **Figure 28b**. In **Figure 29**, glass/fluorine-doped tin oxide (FTO) substrates coated with PEDOT:PSS and PANI-CSA both demonstrated transmittance over 80% in the 400 to 800 nm spectral range, which corresponds to the absorption range of the perovskite

layer. As shown by the spectra, most of the optical loss occurs when the light passes through the glass and FTO layers. The conducting polymer HTLs have an extremely high transparency, which minimizes optical losses.

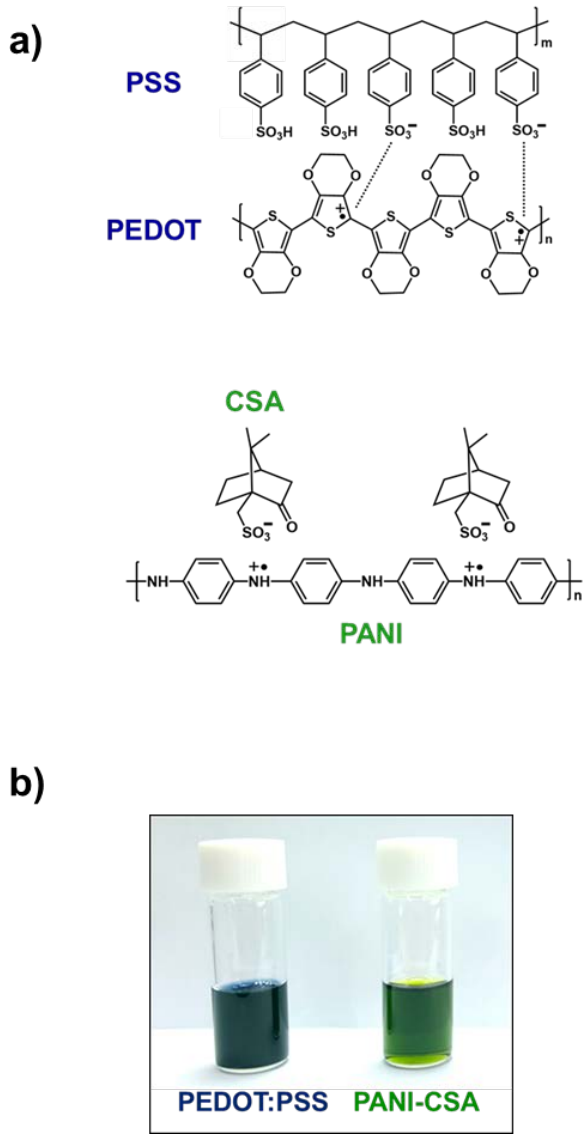

Figure 28. (a) The molecular structure of PEDOT:PSS and PANI-CSA. (b) Digital photograph of PEDOT:PSS and PANI-CSA dispersion solutions.

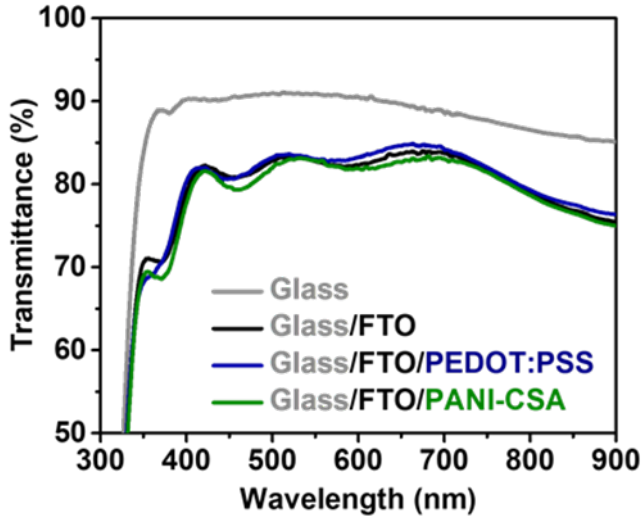

Figure 29. Transmittance spectra of glass, glasss/FTO, and glass/FTO/PEDOT:PSS or PANI-CSA.

3.2.2. Characterization of perovskite films deposited on PEDOT:PSS and PANI-CSA HTLs

Optical and structural properties of perovskite film deposited on the PEDOT:PSS and PANI-CSA HTLs were investigated. Triple cation perovskite ($Cs_{0.05}MA_{0.16}FA_{0.79}Pb(I_{0.84}Br_{0.16})_3$) was used to obtain a highly crystalline perovskite film with excellent photo- and moisture-stability, processed using a one-step solvent engineering method [62,63]. In **Figure 30**, the absorption spectra of perovskite films on PEDOT:PSS and PANI-CSA indicate a band gap value of 1.55 eV, and no differences are observed between the two samples. The top-view FE-SEM images in **Figure 31** confirm that the perovskite films on both PEDOT:PSS and PANI-CSA were densely packed with 200–400 nm crystallites without any pinholes.

Contrary to absorption spectra and surface morphology, X-ray diffraction (XRD) measurements show a small but meaningful difference between the two perovskite films (**Figure 32**). Both patterns exhibit dominant peaks corresponding to photo-active black perovskite, indicating the high crystallinity of the films. A perovskite precursor solution contained excess PbI_2, which acts as a grain boundary passivation layer and induces larger crystal grains [64]. Both

patterns show a weak peak at 12.8°, corresponding to the (011) plane of PbI_2, as expected. However, for the PEDOT:PSS-based perovskite film, the peak at 12.8° is more intense compared to that of the PANI-CSA-based perovskite film, as shown in **Figure 32b**. This result possibly indicates that redundant PbI_2 is produced by decomposition at the PEDOT:PSS/perovskite interface. Although XRD measurements were conducted using fresh perovskite films, the hygroscopic PEDOT:PSS film absorbed some ambient moisture during the fabrication process, which caused slight perovskite decomposition. Based on absorption spectra, surface morphology, and crystallinity, the quality of both perovskite films seems to be about the same, and therefore the slightly excess PbI_2 by the inherent decomposition would have insignificant impact on the initial device performance. But in terms of stability, it might crucially affect device stability with respect to moisture, by accelerating perovskite degradation. This effect will be discussed later in the result of stability test.

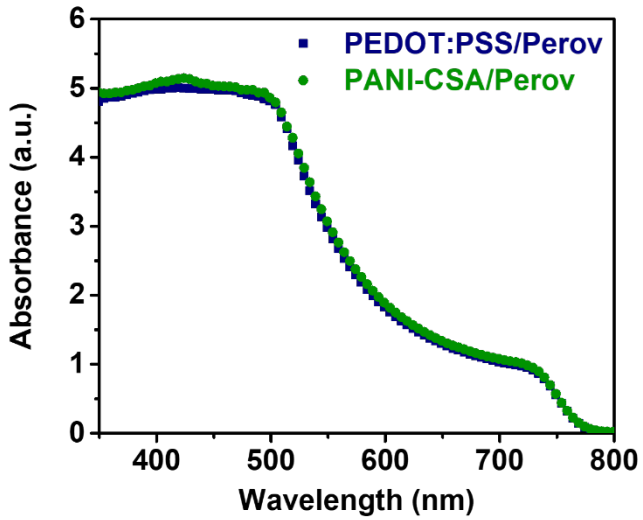

Figure 30. UV-VIS absorption spectra of perovskite films deposited on PEDOT:PSS and PANI-CSA HTLs.

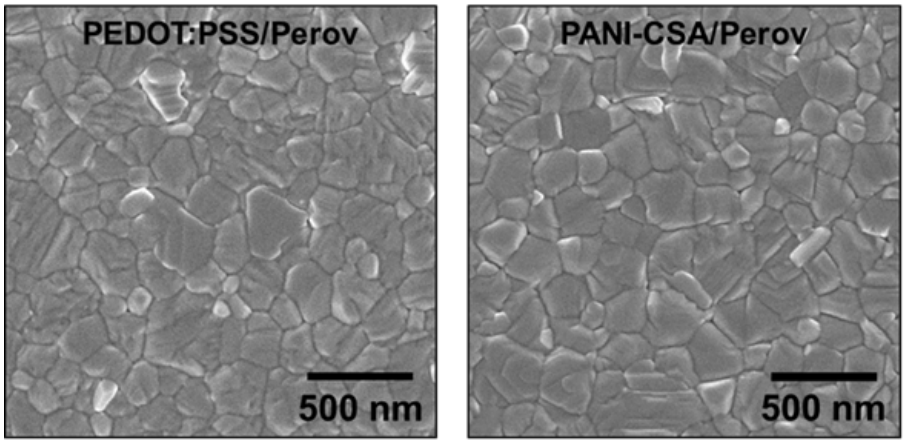

Figure 31. Top-view FE-SEM images of perovskite films deposited on PEDOT:PSS and PANI-CSA HTLs.

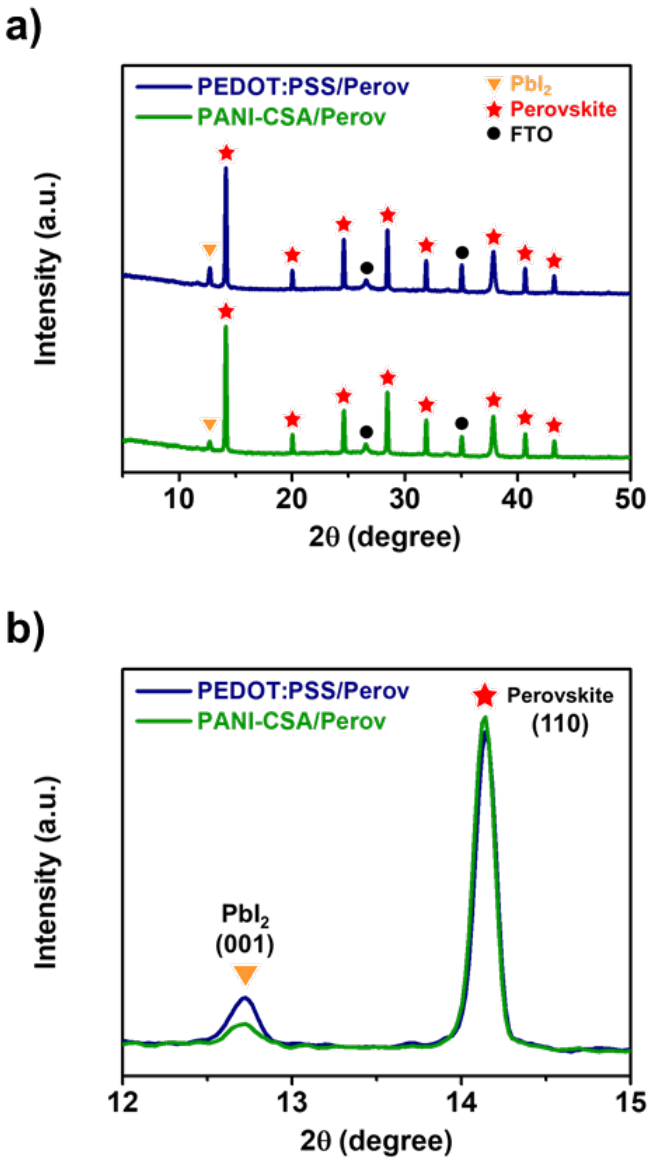

Figure 32. XRD patterns of perovskite film deposited on PEDOT:PSS and PANI-CSA: (a) whole patterns and (b) enlarged patterns with 2θ from 12° to 15°.

3.2.3. Photovoltaic performance of the fabricated PSCs

After investigation of the optical properties, morphology, and crystallinity of the perovskite layer, photovoltaic performances and optoelectronic properties of devices were evaluated. The architecture of the inverted PSCs is illustrated in **Figure 33a**, where PEDOT:PSS or PANI-CSA is employed as the HTL, and PCBM is employed as the ETL. The devices were fabricated on FTO, which has higher conductivity and better thermal stability than ITO [65]. The energy level alignments of the component layers are presented in **Figure 33b**. The work functions of FTO, PEDOT:PSS, and PANI-CSA are calculated from the ultraviolet photoelectron spectroscopy (UPS) measurement, as shown in **Figure 34**. Work function of the samples was determined by equation $\Phi = h\omega - \left| E_{sec} - E_{FE} \right|$, where $h\omega$= 21.2 eV (He(I) source), E_{sec} is the onset of the secondary emission, and E_{FE} is the Fermi edge. The Fermi edge was set to 0 eV.

Figure 35 display the *J–V* characteristic of PSCs with PEDOT:PSS and PANI-CSA HTLs. The average value and distribution of various photovoltaic parameters are summarized in **Table 4** and **Figure 36**, respectively. The device fabricated with PEDOT:PSS had a PCE of 13.76%, a V_{OC} of 0.93 V, a J_{SC} of 21.03 mA cm^{-2}, and a FF of 0.70 for

reverse scan conditions. The efficiency was ~0.75% lower for forward scan due to the hysteresis effect (**Figure 35a**). The device fabricated with PANI-CSA achieved a PCE of 15.19% with enhanced J_{SC} (21.74 mA cm^{-2}) and FF (0.75). Notably, the efficiency discrepancy between the reverse and forward scan is only 0.27%. The maximum PCE was 15.42% and the corresponding *J–V* curve is presented in **Figure 37**. The improvements in photovoltaic parameters and hysteresis behavior suggest that PANI-CSA has an excellent hole transport ability, which is discussed further in later. The PANI-CSA HTL was optimized by varying the concentration of dispersion and the device processed with 0.5 mg mL^{-1} dispersion exhibited the highest efficiency (**Figure 38a** and **Table 5**). The protonation level, depending on the CSA dopant ratio, was also optimized (**Figure 38b** and **Table 6**). To obtain highly conductive PANI film, synthesized PANI (hydrochloric acid-doped) is dedoped with ammonia and re-doped with CSA. Dedoped (un-protonated) PANI, which is EB form, has an insulating nature, and protonation by CSA molecules induces charge carrier delocalization along the polymer backbone and achieves conductive ES form. In this step, the degree of protonation level in PANI can be controlled by molar ratio of CSA to repeat unit. “1/2-doped” stands for the

protonation of one nitrogen atom in repeat unit and “fully-doped” stands for the protonation of two nitrogen atom in repeat unit. It is reported that this protonation level (doping level) of PANI is directly related to the conductivity, optical transparency, and work function [66,67]. Thus, three kinds of PANI-CSA with the varied protonation level (1/2, 3/4, and full) were prepared to test their hole transport ability. Fully-doped PANI-CSA shows the best performance as HTL for PSCs. Fully-doped PANI-CSA has the highest conductivity since bipolaronic form of PANI is favorable for expanded coil conformation and longer charge carrier delocalization and it might positively affect the device performance [66,67].

The reliability of the devices was further investigated by measuring steady-state photo-current density at the maximum power point. In **Figure 39a**, both devices stabilize within a few seconds and remain stable during 300 s of light exposure, and their stabilized current density and efficiency are consistent with the *J–V* characteristics. However, the photo-current densities measured under the light on/off cycle show different transient behavior (**Figure 39b**). The current density of the device fabricated with PANI-CSA reaches a steady-state maximum faster than the device fabricated with PEDOT:PSS. When

the light is off, the current density of the device fabricated with PANI-CSA rapidly drops back to 0 mA cm^{-2}, while the reference device shows some relaxation of the photo-current. In addition, the response of the device fabricated with PANI-CSA is the same for both the first and second illumination cycles, whereas the response of the device fabricated with PEDOT:PSS declines with the second illumination cycle. The instantaneous and stable response of the device fabricated with PANI-CSA can be ascribed to reduced charge accumulation, promoted by the superior hole transport ability of PANI-CSA and reduced defects at the HTL/perovskite interface [68,69].

Contrary to sol-gel processed metal oxide, which requires high temperature sintering over 300 °C, conducting polymers are processed at low temperature [70]. As all annealing treatments in the PSC fabrication procedures are conducted at temperatures under 120 °C, it is possible to employ a polymer/ITO substrate in place of a glass/FTO substrate. Thus, a flexible device was fabricated with a polyethylene terephthalate (PET)/ITO/PANI-CSA/perovskite/PCBM/Au structure, and yielded a PCE of 11.84%, a V_{OC} of 0.88 V, a J_{SC} of 21.33 mA cm^{-2}, and an FF of 0.63 (**Figure 40**). Despite efficiency loss from the inevitable fractures in the perovskite and charge transport layers, the

flexible PSC exhibited good performance, with a PCE over 10%, demonstrating the versatility of PANI-CSA HTLs [71].

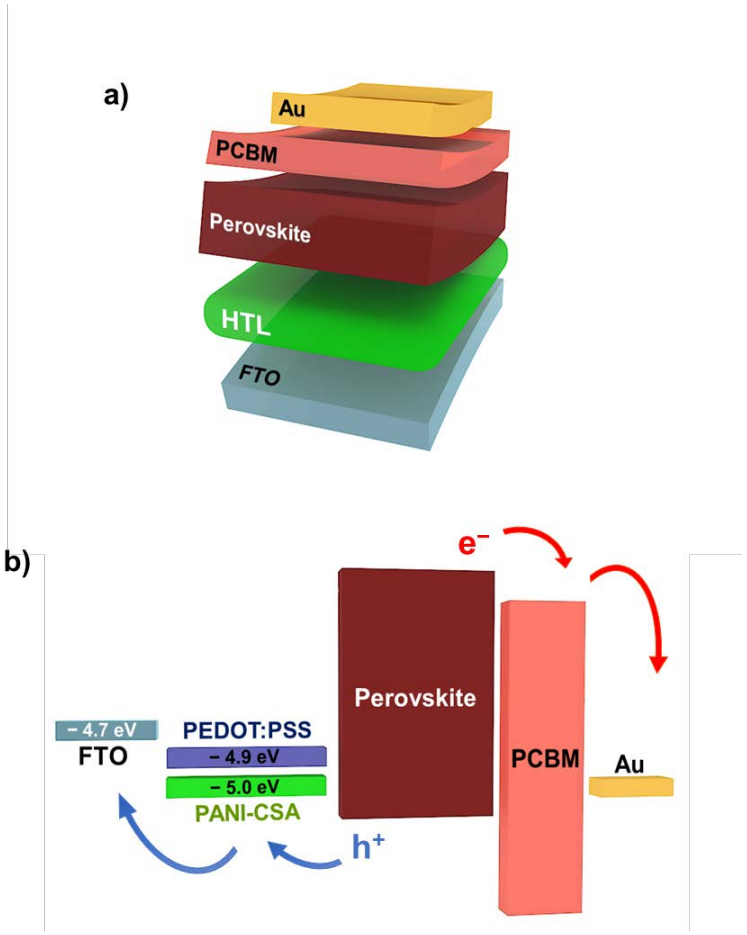

Figure 33. (a) Schematic illustration of the PSC architecture. (b) Energy level diagram of the component layers in the PSC.

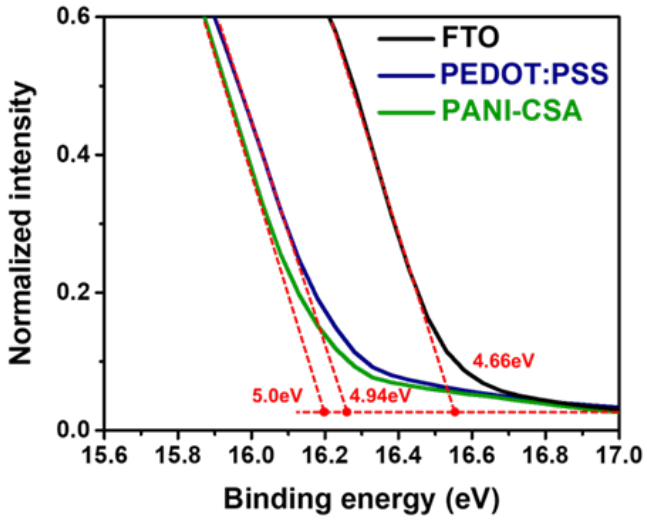

Figure 34. UPS of FTO, PEDOT:PSS, and PANI-CSA. The spectra show the secondary cut-off region and circles indicate the cut-off position.

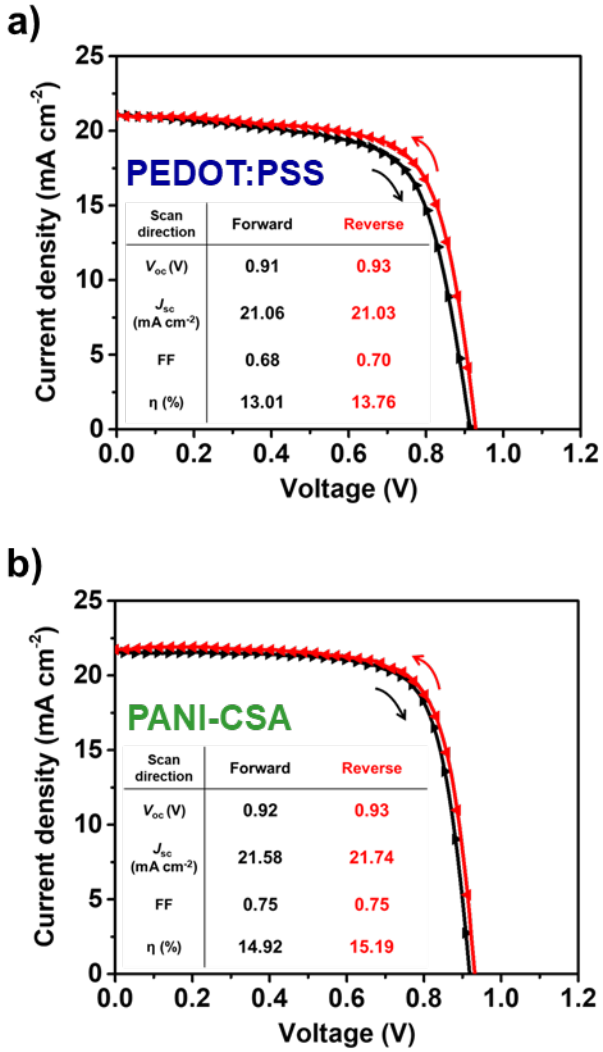

Figure 35. *J–V* characteristics for PSCs using (a) PEDOT:PSS and (b) PANI-CSA HTLs, depending on scan direction.

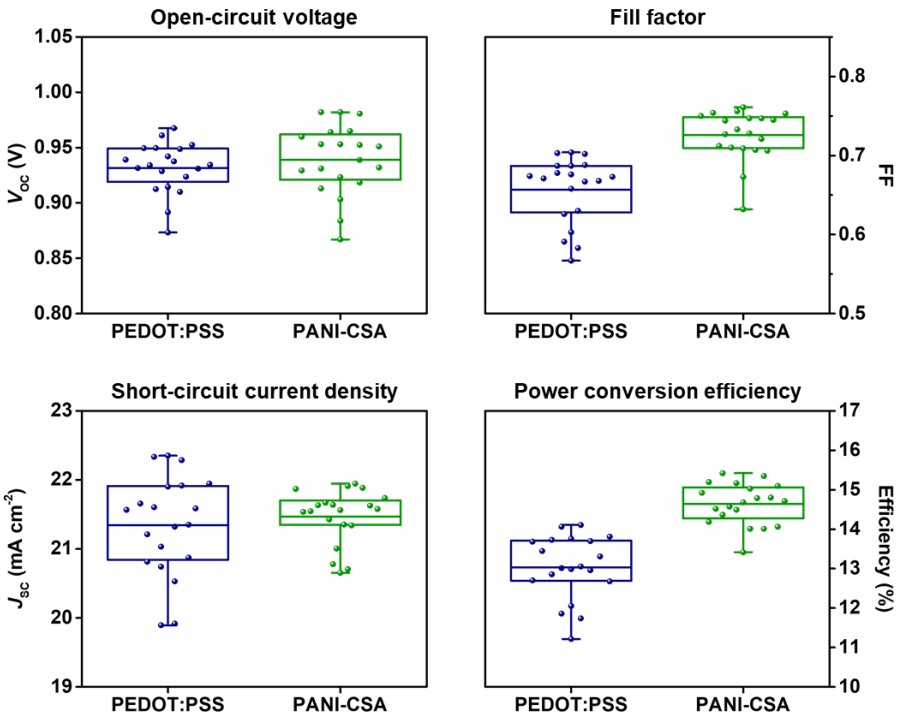

Figure 36. Distribution of photovoltaic parameters (V_{OC}, FF, J_{SC}, and PCE) of PSCs using PEDOT:PSS and PANI-CSA HTLs. The mean values are expressed as solid line inside of the boxes.

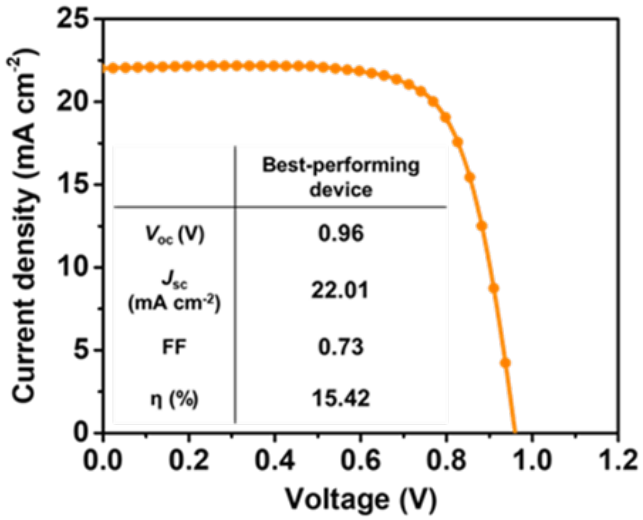

Figure 37. *J–V* characteristic for the best-performing device with PANI-CSA HTL.

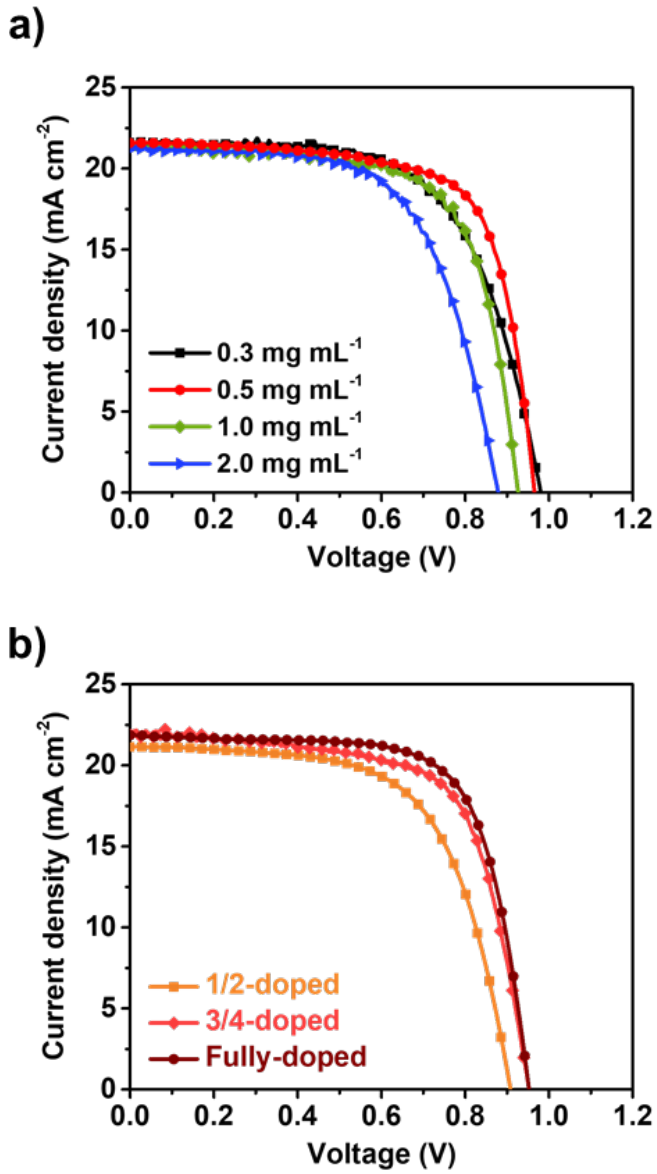

Figure 38. Comparison of *J*–*V* characteristic for PSCs using PANI-CSA HTL depending on (a) concentration and (b) protonation level of PANI-CSA dispersion.

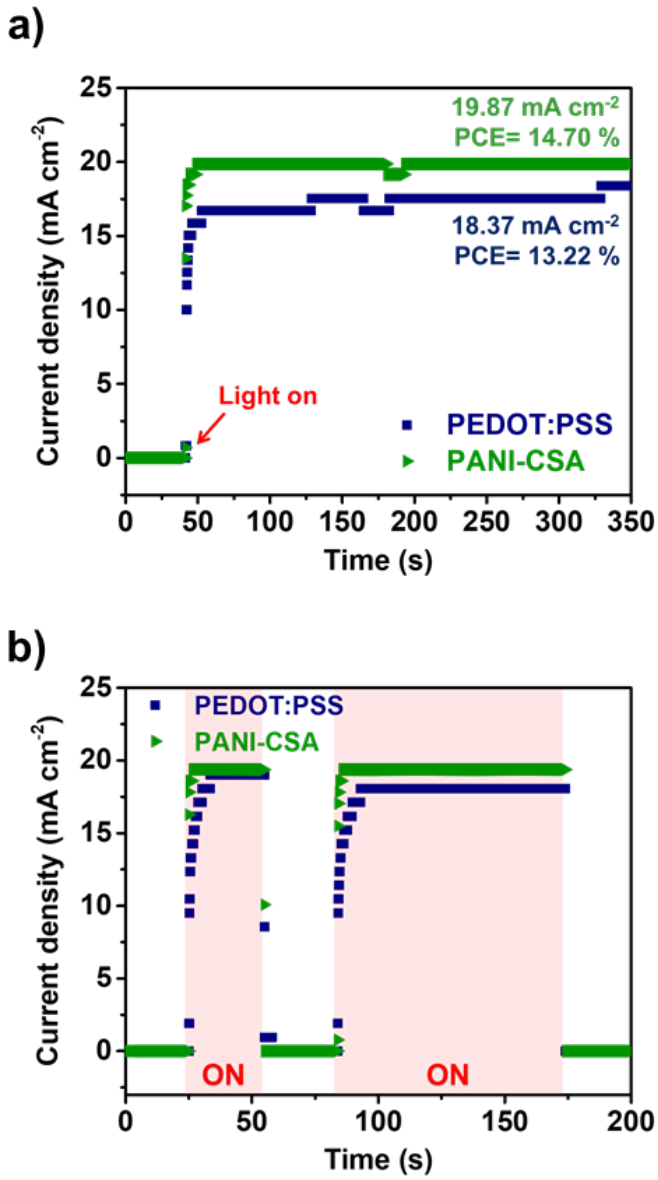

Figure 39. (a) Steady-state photocurrent density of PSCs measured at maximum power voltage (0.72 and 0.74 V for PEDOT:PSS and PANI-CSA, respectively) under (a) continuous illumination and (b) light on/off cycles.

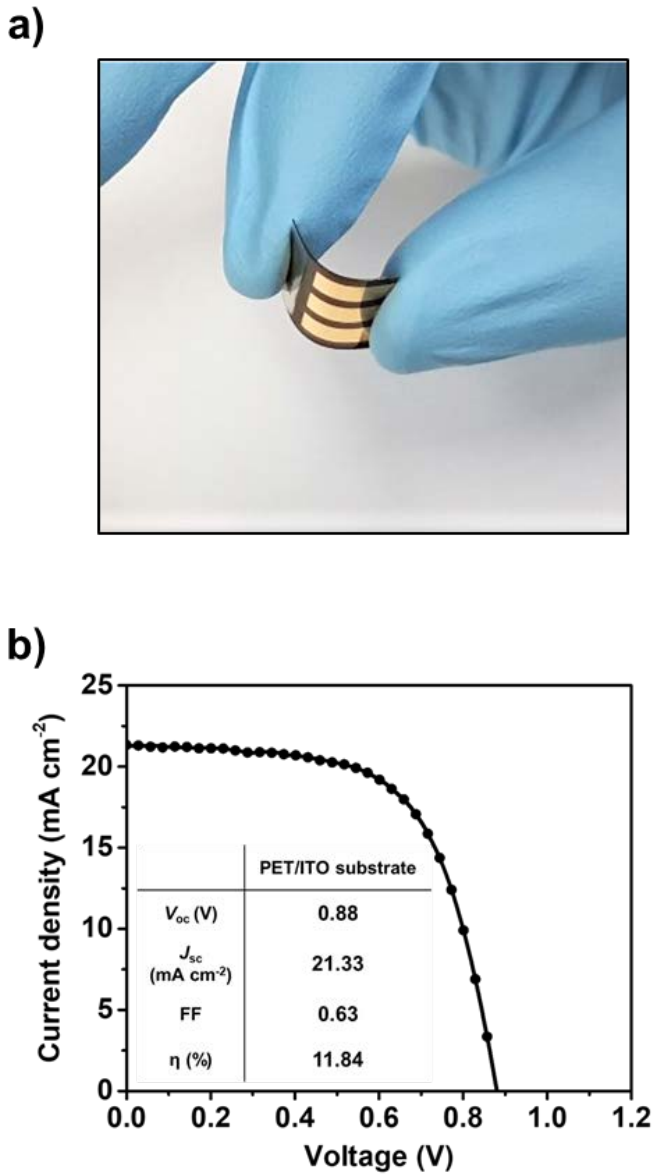

Figure 40. (a) Digital photograph and (b) *J–V* characteristic for flexible PSC using PANI-CSA HTL.

Table 4. Photovoltaic parameters of PSCs using PEDOT:PSS and PANI-CSA HTLs.

HTL	V_{OC}[a] (V)	J_{SC}[a] (mA cm^{-2})	FF[a]	η_{avg}[a] (%)	η_{max} (%)
PEDOT:PSS	0.93	21.34	0.66	13.03	14.11
PANI-CSA	0.94	21.47	0.72	14.64	15.42

[a] Average values of the parameters were obtained for 20 devices.

Table 5. Photovoltaic parameters of PSCs using PANI-CSA HTL depending on concentration of PANI-CSA dispersion.

Concentration (mg mL^{-1})	V_{OC} (V)	J_{SC} (mA cm^{-2})	FF	η (%)
0.3	0.98	21.63	0.63	13.41
0.5	0.97	21.55	0.71	14.80
1.0	0.92	21.30	0.69	13.66
2.0	0.84	21.19	0.66	11.69

Table 6. Photovoltaic parameters of PSCs using PANI-CSA HTL depending on protonation level of PANI.

Protonation level	V_{OC} (V)	J_{SC} (mA cm^{-2})	FF	η (%)
1/2-doped	0.91	21.14	0.63	12.11
3/4-doped	0.95	21.94	0.67	14.06
Fully-doped	0.95	21.86	0.71	14.71

3.2.4. Hole transport ability of PEDOT:PSS and PANI-CSA HTLs

To identify the origin of the outstanding hole transport ability of PANI-CSA, the direct current (DC) conductivity and charge mobility of HTLs were measured from current–voltage (*I–V*) characteristics of the FTO/PEDOT:PSS or PANI-CSA/Au configuration. In the ohmic region of the *I–V* curve (**Figure 41a**), the DC conductivities (σ_0) of each HTL were calculated using the equation $I = \sigma_0 A d^{-1} V$, where A is the active area and d is the thickness of the HTL [72]. The active area was 0.09 cm^2 and the film thicknesses of PEDOT:PSS and PANI-CSA were verified to be 41 and 39 nm, respectively, using the AFM profile system (**Figure 42**). The calculated conductivity of PEDOT:PSS was 3.50×10^{-3} mS cm^{-1}, whereas PANI-CSA had a higher conductivity of 4.33×10^{-3} mS cm^{-1}. In **Figure 41b**, the curves in the space-charge-limited current (SCLC) region, which is beyond the ohmic region, are fitted via the Mott-Gurney law ($J = (9/8)\mu\varepsilon_0\varepsilon(V^2/d^3)$, where μ, ε_0, ε, and d are the charge mobility, free space permittivity, relative dielectric constant, and film thickness, respectively) to determine the charge mobility. The PANI-CSA charge mobility was calculated to be 1.29×10^{-5} cm^2 V^{-1} s^{-1}, which is higher than that of PEDOT:PSS (6.86×10^{-6} cm^2 V^{-1} s^{-1}). As a result, it is conjectured that PANI-CSA

can extract photo-generated holes more efficiently and achieve charge-carrier balance. To validate this hypothesis, charge-carrier dynamics at the HTL/perovskite interface were investigated through time-resolved PL measurement (**Figure 43**). Measurements were taken for the glass/perovskite, glass/PEDOT:PSS/perovskite, and glass/PANI-CSA/perovskite samples. Time-resolved PL spectra were well-fitted with a bi-exponential decay function. The obtained parameters are summarized in **Table 7**. It is clear that the PL lifetime for the glass/PANI-CSA/perovskite sample (τ_{avg} = 8.9 ns) decreased compared to the glass/PEDOT:PSS/perovskite sample (τ_{avg} = 16.0 ns), indicating more effective charge extraction by PANI-CSA, as expected based on high conductivity and charge mobility. EIS analysis was carried out to further characterize the charge transfer in the full devices (**Figure 44**). The spectra were fitted by the equivalent circuit model presented in the figure, and the fitted parameters are summarized in **Table 8**. The R_{CT}, corresponding to the semicircle in the high-frequency region, represents the charge transfer resistance of the devices and is generally related to FF [73]. The only difference between the devices is the HTL. Therefore, the lower R_{CT} value of the device with PANI-CSA represents reduced energy loss during the

charge transport process through FTO/PANI-CSA/perovskite relative to FTO/PEDOT:PSS/perovskite. This result is consistent with the remarkable improvement of the FF in the *J*–*V* characteristic.

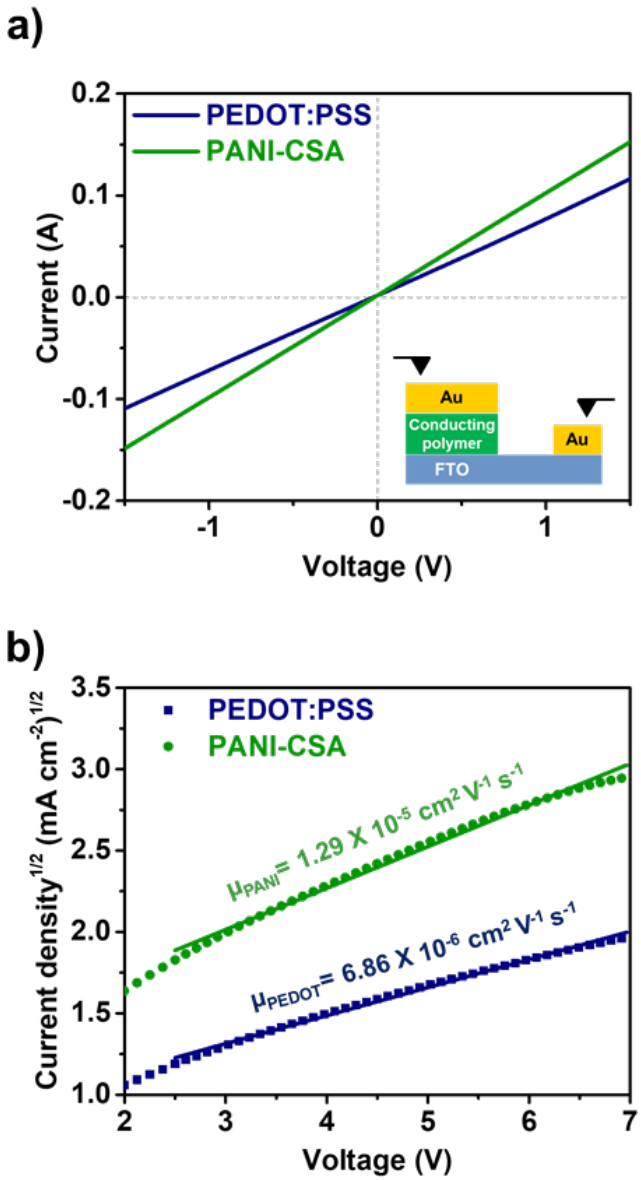

Figure 41. (a) *I–V* characteristics for FTO/PEDOT:PSS and PANI-CSA/Au samples. (b) The SCLC region of $J^{1/2}$–*V* characteristics for FTO/PEDOT:PSS and PANI-CSA/Au and the calculated charge mobility (μ).

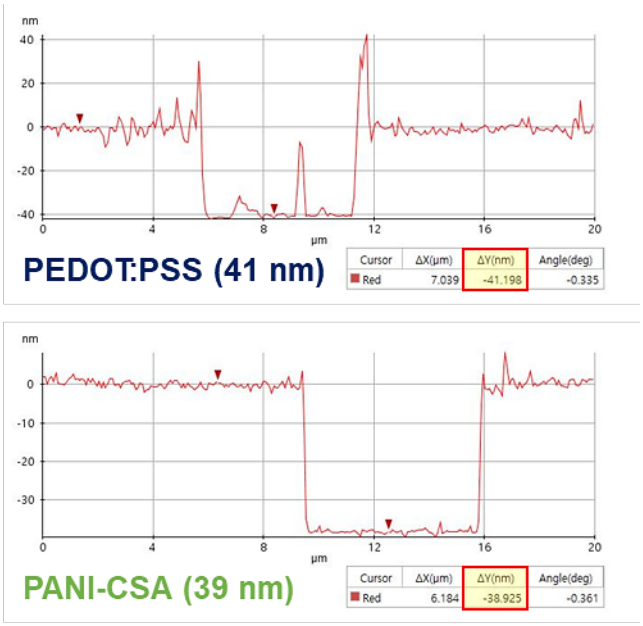

Figure 42. Line profiles of PEDOT:PSS and PANI-CSA films obtained from AFM system.

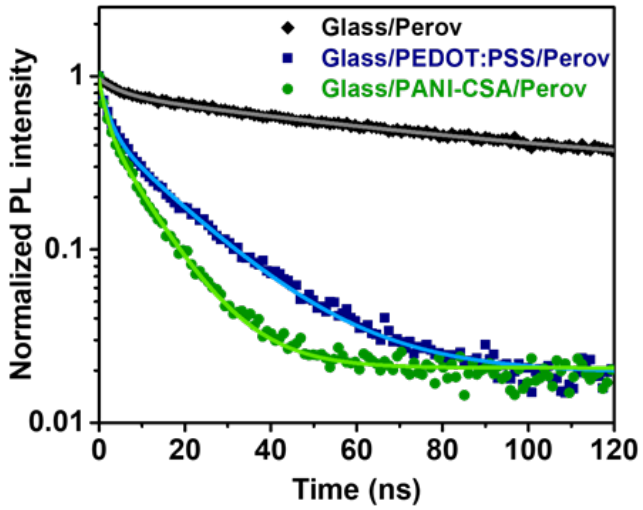

Figure 43. Time-resolved PL decay curves for perovskite films deposited on PEDOT:PSS and PANI-CSA. The samples were excited from the glass side by light irradiation at 520 nm and decay curves were acquired through 665 nm long pass filter.

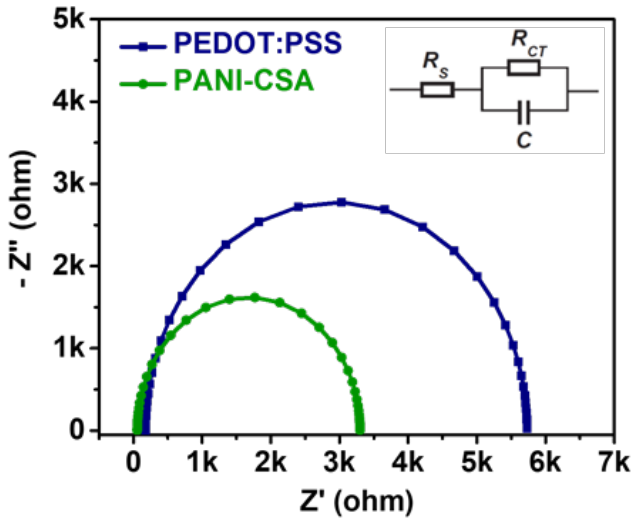

Figure 44. Nyquist plots for the PSCs with PEDOT:PSS and PANI-CSA measured in the dark with a bias of 0.8 V. The frequency scan ranged from 1 Hz to 3 MHz. The inset shows the equivalent circuit.

Table 7. Time-resolved PL decay parameters for glass/none or PEDOT:PSS or PANI-CSA/perovskite samples.

Sample configuration	τ_1 (ns)	τ_2 (ns)	τ_{avg}[a] (ns)	A_1	A_2
Glass/perovskite	5.1	90.6	89.7	0.12	0.55
Glass/PEDOT:PSS/perovskite	2.3	18.0	16.0	0.56	0.49
Glass/PANI-CSA/perovskite	1.7	10.1	8.9	0.52	0.54

[a] $\tau_{avg} = \Sigma_i A_i\tau_i^2 / \Sigma_i A_i\tau_i$

Table 8. EIS parameters of PSCs with PEDOT:PSS and PANI-CSA, obtained by fitting the Nyquist plots.

HTL	R_S (Ω)	R_{CT} (Ω)
PEDOT:PSS	176	5.55×10^3
PANI-CSA	56	3.24×10^3

3.2.5. Ambient stability of PSCs using PEDOT:PSS and PANI-CSA HTLs

Because hygroscopic PEDOT:PSS is generally used underneath the moisture-vulnerable perovskite layer of PSCs, poor air stability can be a critical issue [74]. The ambient stability of the un-encapsulated devices was tested for a month under ambient conditions (temperature = 25 °C, relative humidity = 40 ± 5%). As shown in **Figure 45**, after 10 days of air exposure, the PCE of the reference device fabricated with PEDOT:PSS was only ~35% of the original value, and efficiency was so severely degraded that the device ceased to work. This degradation tendency is similar to results reported by other PEDOT:PSS-based PSC studies [71,75]. On the other hand, the device fabricated with PANI-CSA demonstrated superior stability and maintained 75% of the initial PCE after the month-long test. The *J–V* characteristics and related photovoltaic parameters of the devices before and after the stability test are displayed in **Figure 46** and **Table 9**, respectively. The significantly enhanced stability of the PANI-CSA device can be attributed to the stable interface of PANI-CSA and perovskite, compared to the interface of hygroscopic PEDOT:PSS and perovskite, as observed by XRD. As shown in **Figure 47**, cross-

sectional FE-SEM images of the PSCs after the stability test verify the hypothesis. After a month of ambient exposure, decomposed domains in the perovskite layer of the PEDOT:PSS-based PSC were observed, marked with yellow arrows in **Figure 47**. This result indicates that the photovoltaic performance degradation of the FTO/PEDOT:PSS/perovskite/PCBM/Au structure primarily originated from the instable PEDOT:PSS/perovskite interface. Conversely, the PANI-CSA device retains a seamless perovskite layer after a month of ambient exposure. PANI-CSA prevented perovskite decomposition by ambient moisture, and greatly improved device stability.

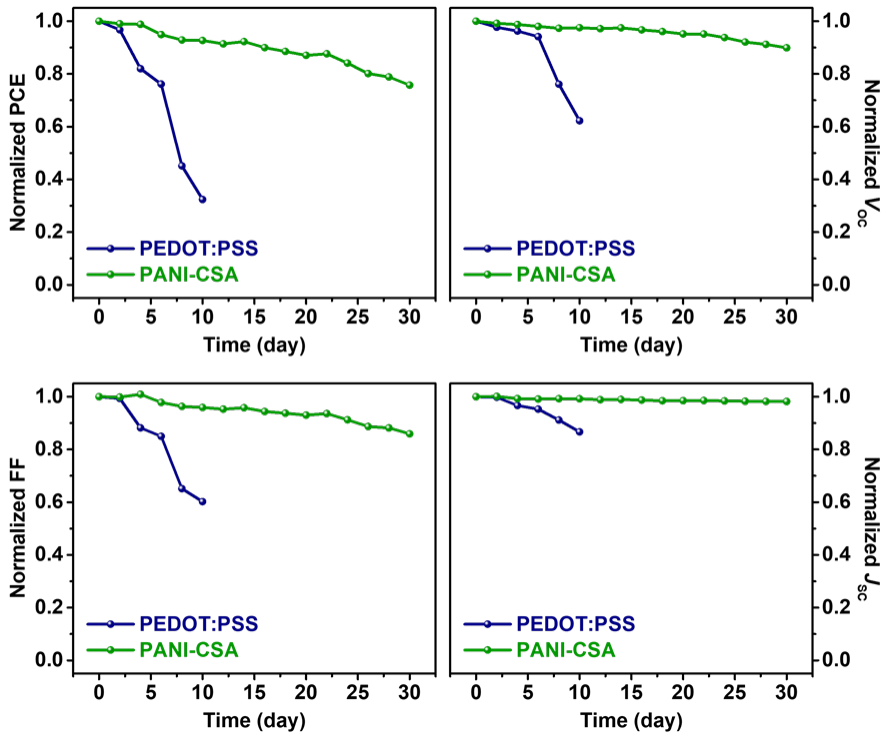

Figure 45. Normalized PCE, V_{OC}, J_{SC}, and FF of the PSCs with PEDOT:PSS and PANI-CSA HTLs as a function of storage time in ambient air (temperature = 25 °C, relative humidity = 40 ± 5%), without encapsulation in the dark.

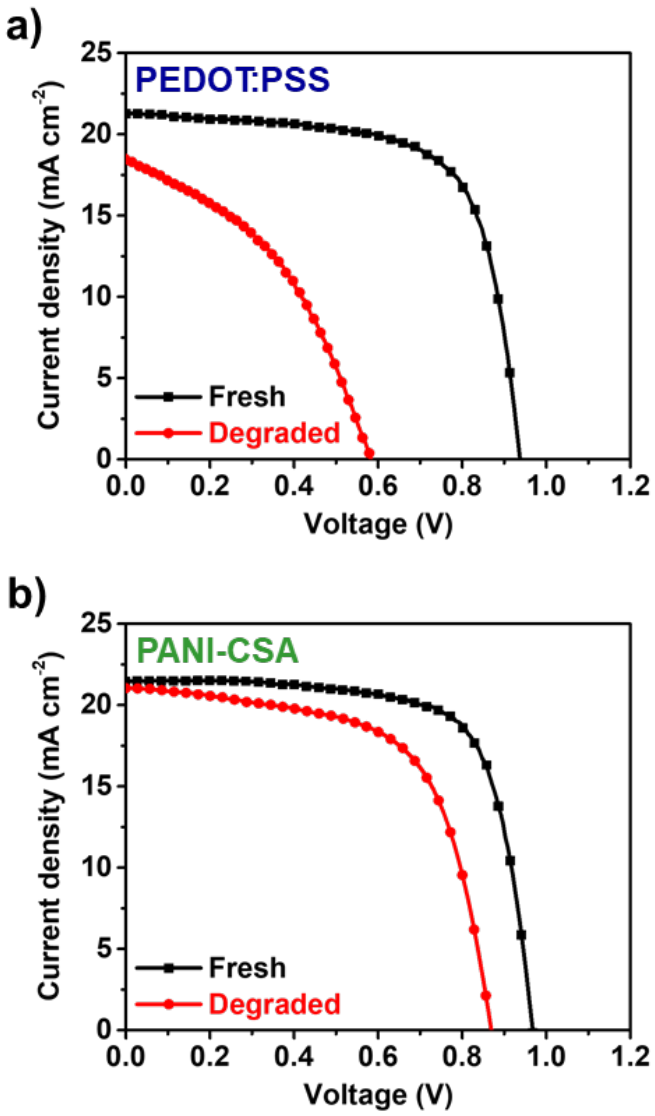

Figure 46. Comparison of *J–V* characteristics for PSCs with (a) PEDOT:PSS and (b) PANI-CSA before and after the stability test.

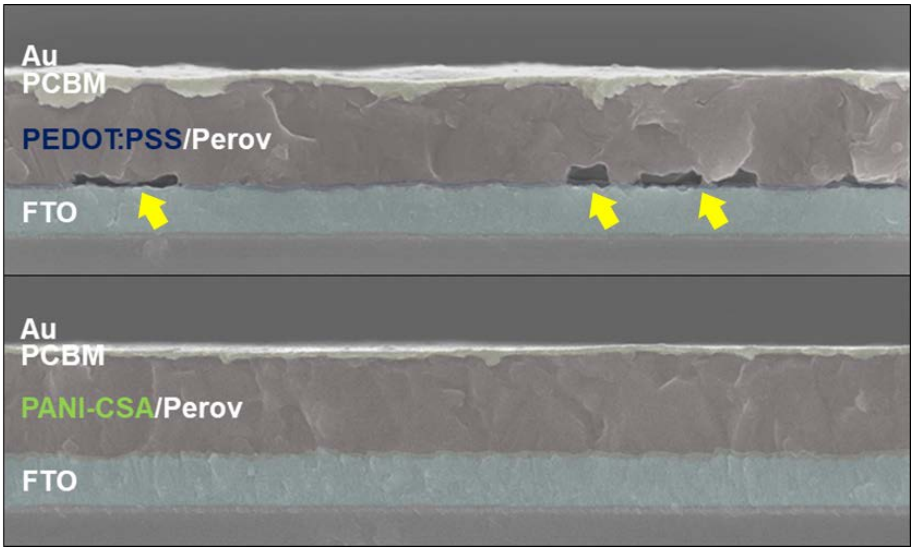

Figure 47. Cross-sectional FE-SEM images of the PSCs after a month-long stability test.

Table 9. Photovoltaic parameters of the PSCs using PEDOT:PSS and PANI-CSA HTLs as a function of storage time in ambient air (temperature = 25 °C, relative humidity = 40 ± 5%).

HTL	Storage time (day)	V_{OC} (V)	J_{SC} (mA cm^{-2})	FF	η (%)
PEDOT:PSS	0	0.93	21.24	0.69	13.70
	10	0.58	18.41	0.41	4.43
PANI-CSA	0	0.96	21.41	0.73	15.09
	30	0.87	21.04	0.63	11.43

3.3. PANI-CSA for HTL of carbon electrode-based PSCs

3.3.1. Fabrication of carbon electrode-based PSCs with PANI-CSA HTL

Figure 48 demonstrates the architecture of carbon electrode-based PSCs with PANI-CSA HTL. To fabricate carbon electrode-based PSCs, compact TiO_2, mesoporous TiO_2, and perovskite layers are processed by the same method with the conventional devices employing spiro-OMeTAD and Au electrode. Triple cation perovskite ($Cs_{0.05}MA_{0.16}FA_{0.79}Pb(I_{0.84}Br_{0.16})_3$) was used for high efficiency and stability, and its composition contains excess PbI_2 (3 mol%) to passivate grain boundary and induce larger crystal grains [62,64]. The perovskite film was prepared using a one-step solvent engineering method as described in the previous section. Upon the perovskite film, the as-prepared PANI-CSA dispersion was spin-coated to form a ultrathin HTL. PANI-CSA dispersion can be processed onto the deposited perovskite film since m-cresol/chlorobenzene co-solvent rarely decompose perovskite layer. Next, carbon conductive paste, composed of graphite and carbon black, was deposited using the screen-printing method to form a 70 um-thick carbon electrode. FE-SEM image in **Figure 49** shows cross-section of the fabricated PSC

following the method. **Figure 50** presents energy band diagram of the device and charge transport behavior by employing PANI-CSA HTL. It is expected that a higher LUMO level of PANI-CSA would effectively prevent interfacial charge recombination at perovskite/carbon interface and well-matched HOMO level would facilitates the hole transport process.

FE-SEM images in **Figure 51** display the morphology change of perovskite surface by spin-coating PANI-CSA HTL. The pristine perovskite film is densely packed with 200–400 nm crystallites, and shows distinct grain boundaries. After spin-coating PANI-CSA, perovskite film is fully covered with tiny PANI-CSA nanoparticles but still shows grain boundaries. Energy-dispersive X-ray (EDX) analysis was carried out to identify the PANI-CSA HTL (**Figure 52**). Iodine (I), lead (Pb), and sulfur (S) elemental signals were detected from surface of PANI-CSA-coated perovskite film. The signals of I and Pb are attributed to the perovskite film. The signal of S is attributed to sulfur in CSA dopant.

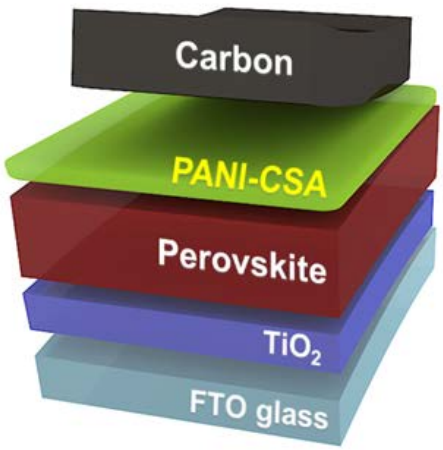

Figure 48. Schematic illustration of the carbon electrode-based PSC with PANI-CSA HTL.

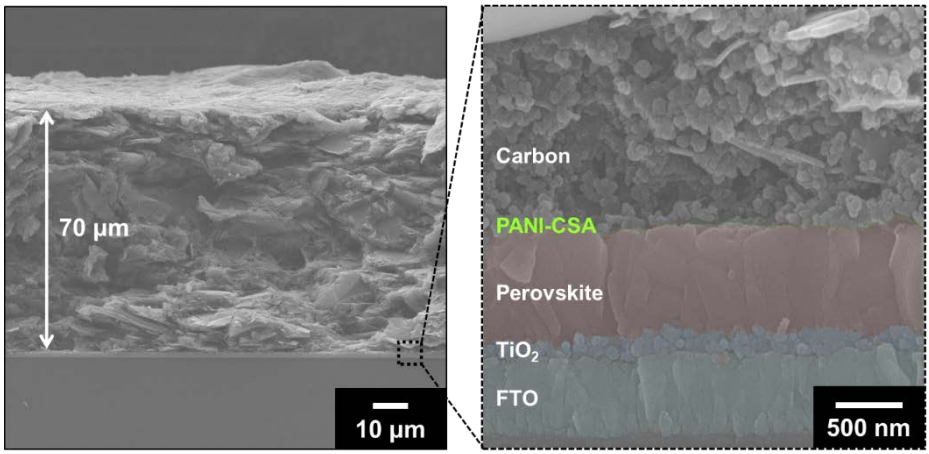

Figure 49. Cross-sectional FE-SEM images of the carbon electrode-based PSC with PANI-CSA HTL.

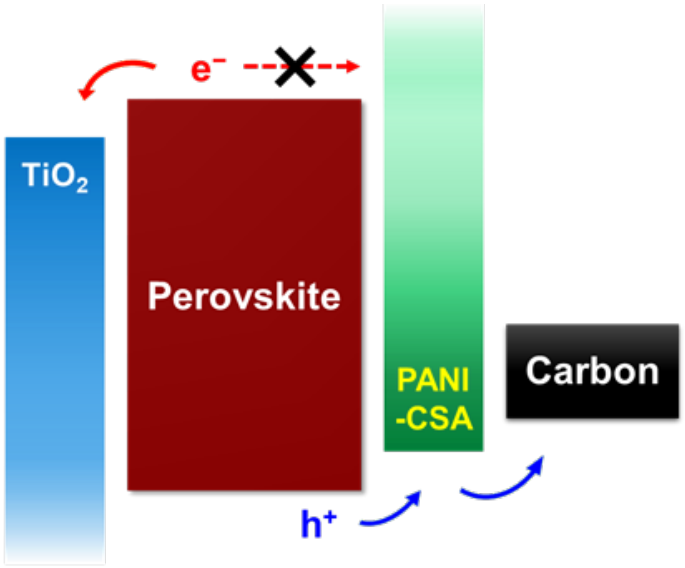

Figure 50. Energy band diagram of each component layer in the fabricated PSC, showing the charge transport of photo-generated carriers.

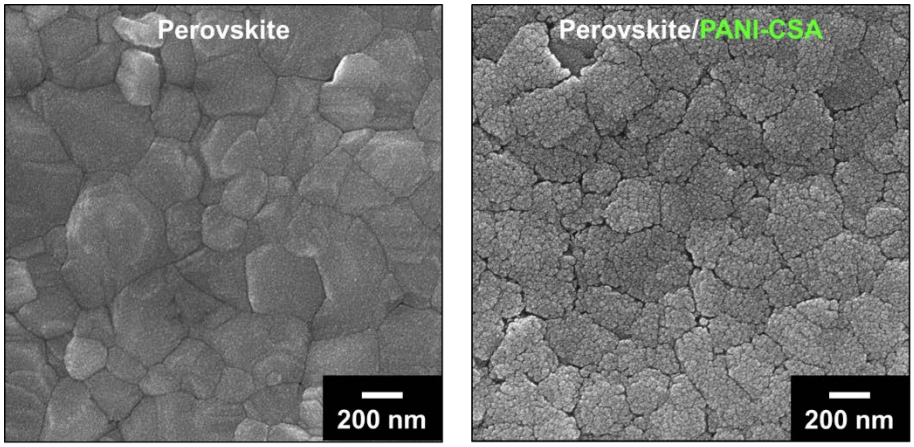

Figure 51. Top-view FE-SEM images of perovskite films without and with PANI-CSA HTL.

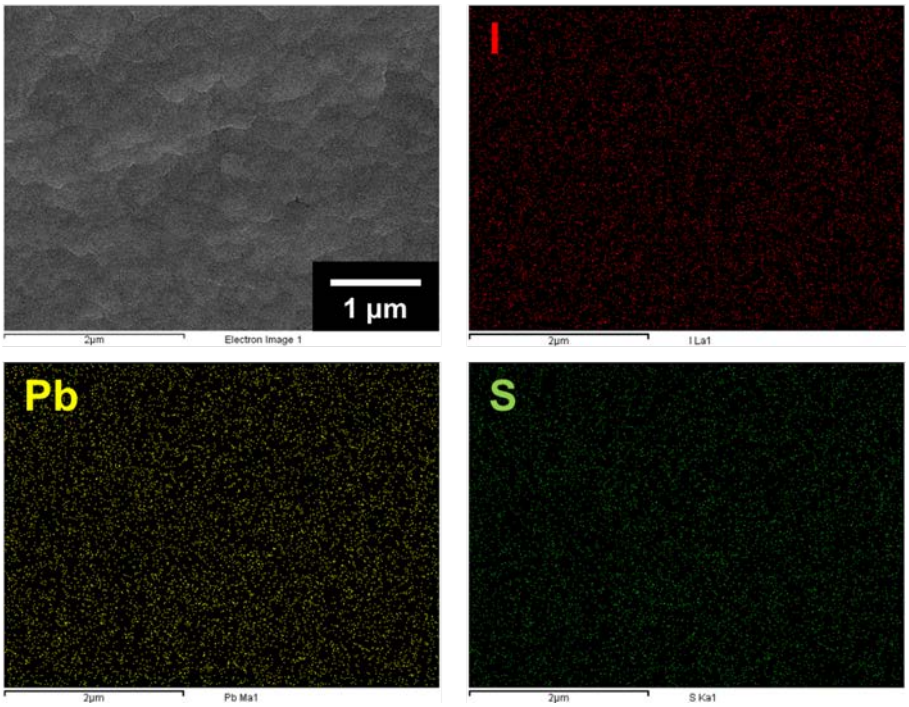

Figure 52. FE-SEM image and EDX elemental mapping for I, Pb, and S from top surface of perovskite/PANI-CSA HTL.

3.3.2. Photovoltaic performance of the fabricated PSCs

The effects of PANI-CSA HTL on the carbon electrode-based PSC performance was investigated. *J–V* curves of devices without (w/o) and with PANI-CSA are presented in **Figure 53**, and the extracted photovoltaic parameters are summarized in **Table 10**. The pristine carbon electrode-based PSC exhibited PCE of 11.46%. With PANI-CSA HTL, the PCE was boosted to 13.17% with improved V_{OC}. Apart from efficiency improvement, it is notable that *J–V* hysteresis was also mitigated by the PANI-CSA HTL ($PCE_{rev–fwd}$= 0.49%) compared to pristine device ($PCE_{rev–fwd}$= 1.36%). Previous studies have reported that the hysteresis behavior of PSCs is primarily originated from the ion migration but can be mitigated by fast charge transport by contacting layers [76,77]. Since PANI-CSA facilitated hole transport from perovskite to carbon, charge accumulation at the perovskite/carbon interface suppressed and the device with PANI-CSA showed less hysteresis behavior. The *J–V* curve of the best-performing device with PANI-CSA HTL is shown in **Figure 54**, which displays PCE of 13.51% with J_{SC} of 21.22 mA cm^{-2}, V_{OC} of 1.02 V, and FF of 0.63. In addition, the device performance for a larger active area of 1 cm^2 was measured. As shown in **Figure 55**, it exhibited PCE of 9.60% with J_{SC} of 20.25

mA cm^{-2}, V_{OC} of 1.03 V, and FF of 0.46.

Stabilized V_{OC} and photocurrent density at maximum power voltage (0.79 V) were measured (**Figure 56**). Stabilized V_{OC} values of devices w/o and with PANI-CSA HTL were 0.97 V and 1.02 V, respectively. In **Figure 56b**, a stabilized photocurrent density of 16.69 mA cm^{-2} and a stabilized PCE of 13.19% were achieved immediately, and remained stable over 300 s under illumination. This result is in good agreement with the *J*–*V* curve, showing the reliability of the device under the operating condition.

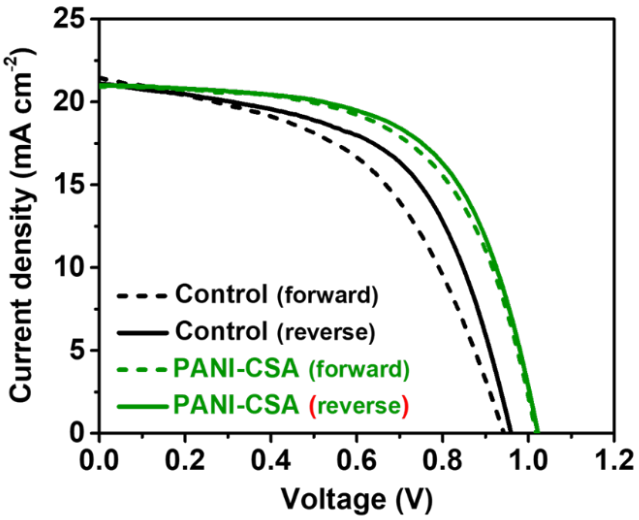

Figure 53. *J–V* characteristics for carbon electrode-based PSCs w/o and with PANI-CSA HTL depending on scan direction.

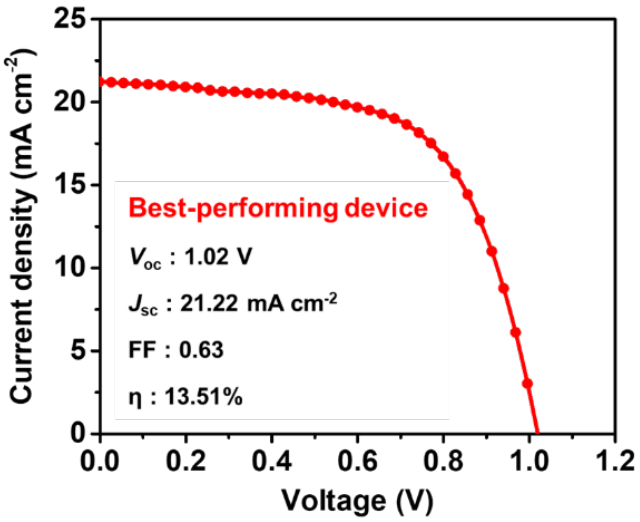

Figure 54. *J–V* characteristics for the best-performing carbon electrode-based PSC with PANI-CSA HTL.

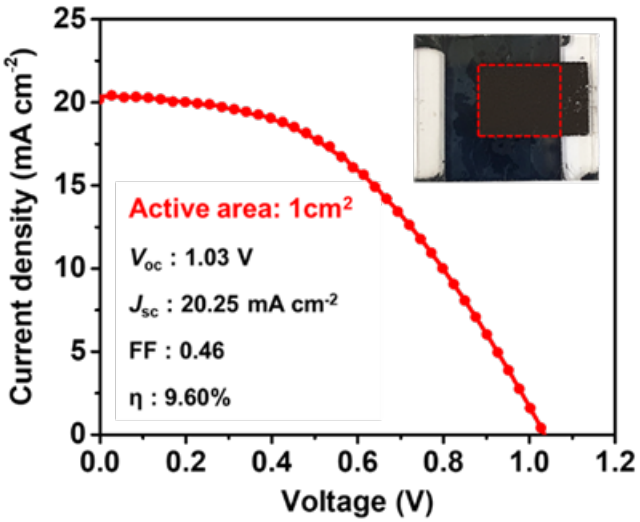

Figure 55. *J–V* characteristic of the device with an active area of 1 cm^2. The inset shows digital photograph of carbon electrode-based PSC with PANI-CSA HTL and the dashed red square represents an active area.

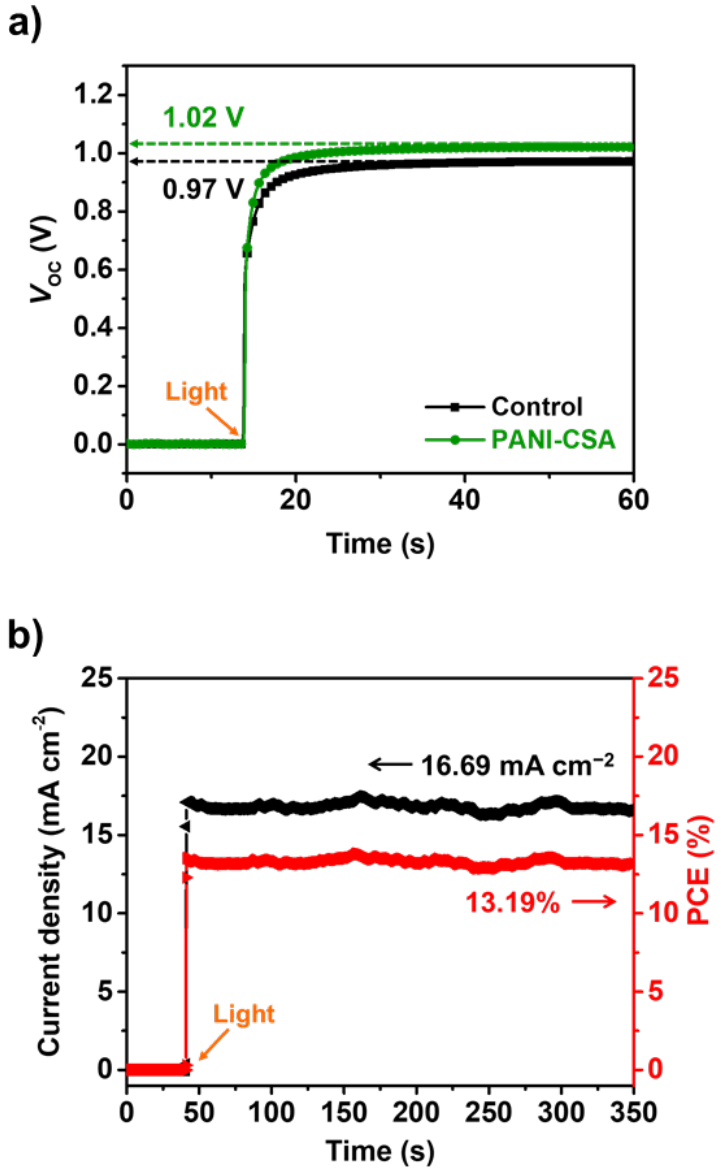

Figure 56. (a) Stabilized V_{OC} of devices w/o and with PANI-CSA HTL. (b) Stabilized photocurrent density and PCE measured at maximum power voltage (0.79 V) of the device with PANI-CSA HTL.

Table 10. Photovoltaic parameters carbon electrode-based PSCs w/o and with PANI-CSA HTL, depending on scan direction.

HTL	Scan direction	V_{OC} (V)	J_{SC} (mA cm^{-2})	*FF*	η (%)
Control	Forward	0.94	21.45	0.50	10.10
	Reverse	0.96	21.12	0.57	11.46
PANI-CSA	Forward	1.02	20.93	0.59	12.68
	Reverse	1.02	20.10	0.61	13.17

3.3.3. Hole transport ability of PANI-CSA in carbon electrode-based PSC

It is supposed that the improvement of device performance is originated from the optimum band alignment by insertion of PANI-CSA HTL. In detail, well-matched HOMO level and higher LUMO level of PANI-CSA enabled faster hole transport and less charge recombination at perovskite/carbon interface. To validate this hypothesis, time-resolved PL decay measurements were performed (**Figure 57a**). The samples were prepared on glass and excited from the glass side by light irradiation at 405 nm. The PL decay curves are fitted with a bi-exponential decay function and the fitted parameters are summarized in **Table 11**. The average PL lifetime (τ_{avg}) was estimated from the obtained two time components (τ_1 and τ_2) according to the equation in **Table 11**. The τ_{avg} was shortened from 94.3 ns to 82.9 ns by contacting the perovskite film with carbon electrode. It indicates that excited charges in the perovskite film were transported to carbon electrode and radiative recombination decreased. When inserting PANI-CSA HTL, sample exhibited a more shortened τ_{avg} (58.7 ns) compared to the other samples. This dramatically quenched PL lifetime is attributed to efficient hole transport by the favorable band alignment

of perovskite/PANI-CSA/carbon structure.

EIS measurements were conducted to further characterize the interfacial charge transport and recombination dynamics in the devices. **Figure 57b** presents Nyquist plots in the frequency range from 1 MHz to 1 Hz under 1 sun illumination at a bias of 1.0 V. The results were fitted by an equivalent circuit model shown in the figure, and the fitted parameters are summarized in **Table 12**. Apparently, the Nyquist plots shows two main arcs. The first arc at high frequency typically corresponds to charge transport process in HTM or at HTM/electrode interface, but in this case it corresponds to hole transport process at the perovskite/carbon interface [78,79]. The arc at low frequency is related to the interfacial charge recombination [27,78]. The reduced series resistance (R_S) and R_{CT} in the device with PANI-CSA HTL indicate the less resistive energy loss during the charge transport through perovskite/carbon interface and carbon electrode itself. This result should lead to higher FF of the PEAI-treated device, which is consistent with the *J–V* characteristic [27,80]. On the contrary, the device with PANI-CSA HTL exhibited a larger second arc and increased charge recombination resistance (R_{REC}). As all interfaces in the PSCs are constant apart from perovskite/carbon interface, it

represents that interfacial recombination at perovskite/carbon reduced by insertion of PANI-CSA HTL. PANI-CSA HTL effectively prevented electron diffusion into carbon electrode, and contributes to remarkable V_{OC} enhancement.

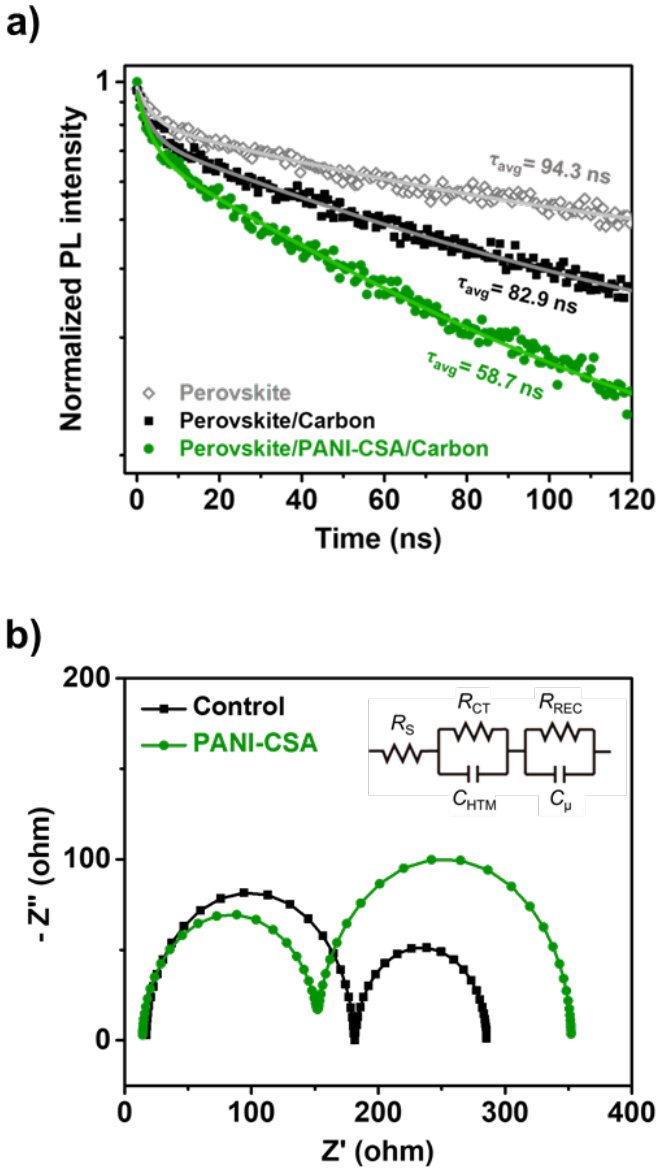

Figure 57. (a) Time-resolved PL decay curves for the samples of glass/perovskite, glass/perovskite/carbon, and glass/perovskite/PANI-CSA/carbon. (b) Nyquist plots for the PSCs w/o and with PANI-CSA HTL.

Table 11. Time-resolved PL decay parameters for glass/perovskite/ none PANI-CSA/carbon samples.

Sample configuration	τ_1 (ns)	τ_2 (ns)	τ_{avg}[a] (ns)	A_1	A_2
Glass/Perovskite	3.7	95.7	94.3	0.18	0.47
Glass/Perovskite/Carbon	3.2	84.1	82.9	0.23	0.56
Glass/Perovskite/PANI-CSA/Carbon	3.4	60.2	58.7	0.26	0.59

[a] $\tau_{avg} = \Sigma_i A_i\tau_i^2 / \Sigma_i A_i\tau_i$

Table 12. EIS parameters of the carbon electrode-based PSCs w/o and with PANI-CSA HTL, obtained by fitting the Nyquist plots.

HTL	R_S (Ω)	R_{CT} (Ω)	R_{REC} (Ω)
Control	14.2	1.64×10^2	1.04×10^2
PANI-CSA	16.9	1.38×10^2	1.99×10^2

3.3.4. Ambient and thermal stabilities of carbon electrode-based PSC with PANI-CSA HTL

Finally, the stability of the devices was examined. To compare with conventional PSCs, the device with FTO/TiO_2/Perovskite/Spiro-OMeTAD/Au structure was fabricated and tested together. Its *J–V* curve and parameters are given in **Figure 58**. Firstly, the long-term stability of the un-encapsulated devices was tested, which were stored in ambient condition (temperature = 25 °C, relative humidity = 40 ± 5%). In **Figure 59a**, The PCE of the conventional device degraded over a month to 75% of its initial performance. The conventional device can suffer from degradations by both the hygroscopic Li-TFSI dopant in HTM and unstable HTM/Au interface [81-83]. However, carbon electrode-based PSCs are free from those hazards and protect perovskite layer with hydrophobic carbon electrode. The carbon electrode-based PSCs w/o and with PANI-CSA HTL retained 86% and 83% of their initial performance after the test, showing outstanding ambient stability. The PCE of the device with PANI-CSA HTL showed slightly larger degradation and it is conjectured that diffused acid from PANI-CSA might negatively affect to the perovskite film.

Beside the long-term stability against ambient moisture, the thermal

stability was also investigated (**Figure 59b**). The performance of the three devices heating at a temperature of 100 °C was checked periodically. During the heating, carbon electrode-based devices maintained their performance or even showed enhanced efficiency due to strengthened perovskite/carbon interface [78]. But the conventional device severely degraded because thermally diffused ions from perovskite to HTM deteriorate the electrical property of spiro-OMeTAD and thermal stress can generate voids near HTM/Au interface.[84,85] Consequently, the results demonstrated that carbon electrode-based PSCs with PANI-CSA HTL have excellent ambient and thermal stability.

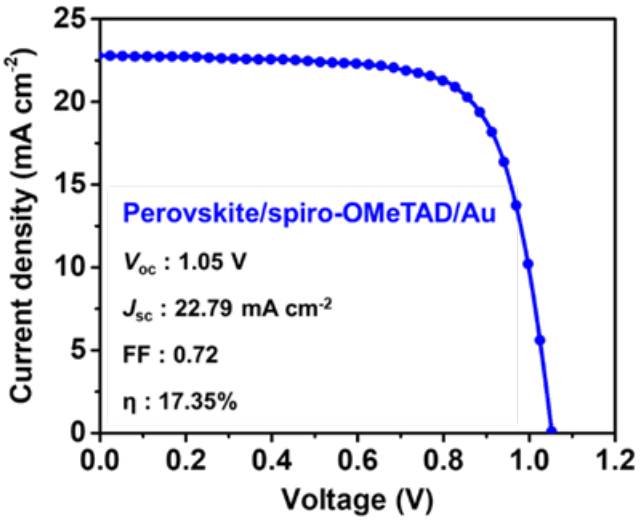

Figure 58. *J–V* characteristic for conventional PSC with structure of FTO/TiO_2/perovskite/spiro-OMeTAD/Au.

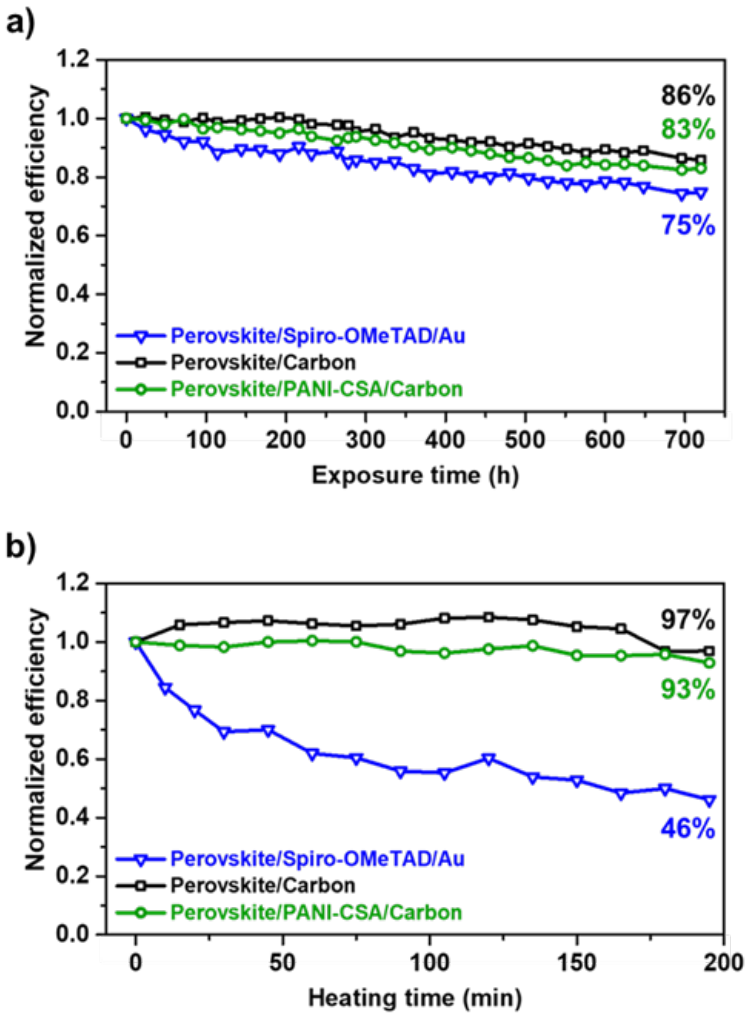

Figure 59. (a) Normalized PCE evolution of conventional PSC with structure of FTO/TiO_2/perovskite/spiro-OMeTAD/Au and carbon electrode-based PSCs w/o and with PANI-CSA, stored in the controlled ambient conditions (temperature = 25 °C, relative humidity = 40 ± 5%). (b) Normalized PCE evolution of the PSCs as a function of heating time at 100 °C.

4. Conclusion

Polyaniline-based hole transport materials were synthesized and successfully employed in two types of PSC architectures: inverted PSC and carbon electrode-based PSC. Solution-processable PANI:PSS and PANI-CSA were prepared by chemical oxidative polymerization and utilized as an HTL. The properties of polyaniline-based HTLs, including a surface morphology, wettability, thickness, and doping level were optimized to improve efficiency and stability of the PSCs. The subtopics are concluded in the view point of each subtopic as follows:

1. PANI:PSS was synthesized, and modified with the surfactant to improve hole transport ability as HTL for inverted PSCs. Triton X–100, a nonionic surfactant, played a bifunctional role to enhance the hole transport capability of PANI:PSS. Firstly, the amphiphilic property of the surfactant lowered the surface tension of a PANI aqueous solution, which enabled the production of a flat, uniformly thick PANI:PSS film. In addition, polyethylene oxide functional groups incorporated in the Triton X–100 induced a phase separation between PANI and PSS, thus revealed conductive domains where the charge transporting species (PANI) were abundant. The PSCs using PANI:PSS with the optimal

surfactant concentration of 1.0 wt% exhibited a significantly increased average PCE (from 6.59 to 10.90%), with a maximum PCE of 11.67%.

2. PANI-CSA was synthesized, and utilized as HTL for inverted PSCs. PANI-CSA exhibited higher conductivity and charge mobility compared to PEDOT:PSS, and these factors led to superb hole transport ability. The PSCs fabricated using PANI-CSA HTL showed an maximum PCE of 15.42% with negligible *J*−*V* hysteresis, which is higher than that of the devices using PEDOT:PSS (14.11%). More importantly, the device stability under ambient moisture conditions was significantly improved by replacing hygroscopic PEDOT:PSS with PANI-CSA. In addition, low-temperature processed PANI-CSA enables fabrication of PSCs on flexible polymer substrates, realizing a high-performance flexible PSC with a PCE of 11.84%.

3. PANI-CSA was introduced as HTL for carbon electrode-based PSCs. The suitable LUMO and HOMO levels of PANI-CSA effectively suppressed charge recombination at perovskite/carbon interfaces and facilitated hole transport process. The carbon electrode-based PSCs with PANI-CSA HTL showed an improved PCE of 13.17%, compared with pristine device without PANI-CSA (11.46%). It is noteworthy that the fabrivated device was highly stable under ambient condition due to

protection of hydrophobic carbon layer. Thermal stability of the device was also excellent, showing no efficiency loss after heating at 100 °C, because thermally unstable spiro-OMeTAD/Au was replaced by PANI-CSA/carbon electrode. The applications of PANI-CSA to various device structures demonstrated its versatility.

References

[1] M. A. Green, A. Ho-Baillie, H. J. Snaith, *Nat. Photon.*, **2014**, 8, 506.

[2] H. S. Jung, N.-G. Park, *Small*, **2015**, 11, 10.

[3] N.-G. Park, *Mater. Today*, **2015**, 18, 65.

[4] W. Zhang, G. E. Eperon, H. J. Snaith, *Nat. Energy.*, **2016**, 1, 16048.

[5] P. Gao, M. Grätzel, M. K. Nazeeruddin, *Energy Environ. Sci*., 2014, **7**, 2448.

[6] M. B. Johnston, L. M. Herz, *Acc. Chem. Res.*, **2016**, 49, 146.

[7] C. Wehrenfennig, G. E. Eperon, M. B. Johnston, H. J. Snaith, L. M. Herz, *Adv. Mater.*, **2014**, 26, 1584.

[8] N. J. Jeon, J. H. Noh, Y. C. Kim, W. S. Yang, S. Ryu, S. I. Seok, *Nat. Mater*., **2014**, 13, 897.

[9] N. J. Jeon, J. H. Noh, W. S. Yang, Y. C. Kim, S. Ryu, J. Seo, S. I. Seok, *Nature*, **2015**, 517, 476.

[10] M. Saliba, T. Matsui, J.-Y. Seo, K. Domanski, J.-P. Correa-Baena, M. K. Nazeeruddin, S. M. Zakeeruddin, W. Tress, A. Abate, A. Hagfeldt, M. Grätzel, *Energy Environ. Sci*., **2016**, 9, 1989.

[11] S. Yue, K. Liu, R. Xu, M. Li, M. Azam, K. Ren, J. Liu, Y. Sun, Z. Wang, D. Cao, X. Yan, S. Qu, Y. Lei, Z. Wang, *Energy Environ. Sci*., **2017**, 10, 2570.

[12] W. S. Yang, B.-W. Park, E. H. Jung, N. J. Jeon, Y. C. Kim, D. U. Lee, S. S. Shin, J. Seo, E. K. Kim, J. H. Noh, S. I. Seok, *Science*, **2017**, 356, 1376.

[13] Y. Chen, L. Zhang, Y. Zhang, H. Gao, H. Yan, *RSC Adv*., **2018**, 8, 10489.

[14] D. Wang, M. Wright, N. K. Elumalai, A. Uddin, *Sol. Energy*

Mater Sol., **2016**, 147, 255.
[15] Y. Chen, S. Yu, Y. Sun, Z. Liang, *J. Phys. Chem. Lett.*, **2018**, 9, 2627.
[16] J. Yan, W. Qiu, G. Wu, P. Heremans, H. Chen, *J. Mater. Chem. A*, **2018**, 6, 11063.
[17] K. T. Cho, G. Grancini, Y. Lee, E. Oveisi, J. Ryu, O. Almora, M. Tschumi, P. A. Schouwink, G. Seo, S. Heo, J. Park, J. Jang, S. Paek, G. Garcia-Belmonte, M. K. Nazeeruddin, *Energy Environ. Sci*., **2018**, 11, 952.
[18] Q. Fu, X. Tang, B. Huang, T. Hu, L. Tan, L. Chen, Y. Chen, *Adv. Sci*., **2018**, 5, 1700387.
[19] W. Chen, L. Xu, X. Feng, J. Jie, Z. He, *Adv. Mater.*, **2017**, 29, 1603923.
[20] K. Lee, J. Ryu, H. Yu, J. Yun, J. Lee, J. Jang, *Nanoscale*, **2017**, 9, 16249.
[21] X. Yin, Z. Yao, Q. Luo, X. Dai, Y. Zhou, Y. Zhang, Y. Zhou, S. Luo, J. Li, N. Wang, H. Lin, *ACS Appl. Mater. Interfaces*, **2017**, 9, 2439.
[22] J. Chen, J.-Y. Seo, N.-G. Park, *Adv. Energy Mater.*, **2018**, 8, 1702714.
[23] K. O. Brinkmann, J. Zhao, N. Pourdavoud, T. Becker, T. Hu, S. Olthof, K. Meerholz, L. Hoffmann, T. Gahlmann, R. Heiderhoff, M. F. Oszajca, N. A. Luechinger, D. Rogalla, Y. Chen, B. Cheng, T. Riedl, *Nat. Commun.*, **2017**, 8, 13938.
[24] H. Chen, S. Yang, *Adv. Mater.*, **2017**, 29, 1603994.
[25] F. Zhang, X. Yang, M. Cheng, W. Wang, L. Sun, *Nano Energy*, **2016**, 20, 108.
[26] A. Mei, X. Li, L. Liu, Z. Ku, T. Liu, Y. Rong, M. Xu, M. Hu, J. Chen, Y. Yang, M. Grätzel, H. Han, *Science*, **2014**, 345, 295.
[27] J. Ryu, K. Lee, J. Yun, H. Yu, J. Lee, J. Jang, *Small*, **2017**, 13,

1701225.
[28] S. Ahn, S.-H. Jeong, T.-H. Han, T.-W. Lee, *Adv. Opt. Mater.*, **2017**, 5, 1600512.
[29] A. J. Heeger, *J. Phys. Chem. B*, **2001**, 105, 8475.
[30] A. G. MacDiarmid, *Angew. Chem. Int. Ed.*, **2001**, 40, 2581.
[31] A. Kausar, *J Macromol. Sci. A.*, **2017**, 54, 640.
[32] Y. Olivier, D. Niedzialek, V. Lemaur, W. Pisula, K. Müllen, U. Koldemir, J. R. Reynolds, R. Lazzaroni, J. Cornil, D. Beljonne, *Adv. Mater.*, **2014**, 26, 2119.
[33] X. Zhao, M. Wang, *Materials Today Energy*, **2018**, 7, 208.
[34] N. Gospodinova, L. Terlemezyan, *Prog. Polym.*, **1998**, 23, 1443.
[35] W. Yan, S. Ye, Y. Li, W. Sun, H. Rao, Z. Liu, Z. Bian, C. Huang, *Adv. Energy Mater.*, **2016**, 6, 1600474.
[36] S. Bhadra, D. Khastgir, N. K. Singha, J. H. Lee, *Prog. Polym. Sci. (Oxford)*, **2009**, 34, 783.
[37] C. O. Baker, X. Huang, W. Nelson, R. B. Kaner, *Chem. Soc. Rev.*, **2017**, 46, 1510-1525.
[38] Y. Xiao, G. Han, Y. Chang, H. Zhou, M. Li, Y. Li, *J. Power Sources*, **2014**, 267, 1.
[39] K.-G. Lim, S. Ahn, H. Kim, M.-R. Choi, D. H. Huh, T.-W. Lee, *Adv. Mater. Interfaces*, **2016**, 3, 1500678.
[40] S. Ameen, M. S. Akhtar, H.-K. Seo, H.-S. Shin, *Langmuir*, **2014**, 30, 12786.
[41] P. K. Kahol, K. K. Satheesh Kumar, S. Geetha, D. C. Trivedi, *Synth. Met.*, **2003**, 139, 191.
[42] K. Lee, S. Cho, M. Kim, J. Kim, J. Ryu, K.-Y. Shin, J. Jang, *J. Mater. Chem. A*, **2015**, 3, 19018.
[43] M. Kim, C. Lee, J. Jang, *Adv. Funct. Mater.*, **2014**, 24, 2489.
[44] A. M. Massari, K. J. Stevenson, J. T. Hupp, *J. Electroanal. Chem.*, **2001**, 500, 185.

[45] B. E. Jaramillo-Tabares, F. J. Isaza, S. I. C. d. Torresi, *Mater. Chem. Phys.*, **2012**, 132, 529.
[46] J. Y. Oh, M. Shin, J. B. Lee, J.-H. Ahn, H. K. Baik, U. Jeong, *ACS Appl. Mater. Interfaces*, **2014**, 6, 6954.
[47] D. Alemu Mengistie, P.-C. Wang, C.-W. Chu, *J. Mater. Chem. A*, **2013**, 1, 9907.
[48] J.-W. Lee, D.-H. Kim, H.-S. Kim, S.-W. Seo, S. M. Cho, N.-G. Park, *Adv. Energy Mater.*, **2015**, 5, 1501310.
[49] D. Yu, Y. Yang, M. Durstock, J.-B. Baek, L. Dai, *ACS Nano*, **2010**, 4, 5633.
[50] S. Aharon, A. Dymshits, A. Rotem, L. Etgar, *J. Mater. Chem. A*, **2015**, 3, 9171.
[51] H. Choi, C.-K. Mai, H.-B. Kim, J. Jeong, S. Song, G. C. Bazan, J. Y. Kim, A. J. Heeger, *Nat. Commun.*, **2015**, 6, 7348.
[52] H.-S. Kim, I.-H. Jang, N. Ahn, M. Choi, A. Guerrero, J. Bisquert, N.-G. Park, *J. Phys. Chem. Lett.*, **2015**, 6, 4633.
[53] C. M. Romero, M. S. Paéz, *Phys. Chem. Liq.*, **2006**, 44, 61.
[54] J.-B. Lee, K. Rana, B. H. Seo, J. Y. Oh, U. Jeong, J.-H. Ahn, *Carbon*, **2015**, 85, 261.
[55] Y. Li, L. Meng, Y. Yang, G. Xu, Z. Hong, Q. Chen, J. You, G. Li, Y. Yang, Y. Li, *Nat. Commun.*, **2016**, 7, 10214.
[56] K. Lee, C.-M. Yoon, J. Noh, J. Jang, *Chem. Commun.*, **2016**, 52, 4231.
[57] W. Sun, Y. Li, S. Ye, H. Rao, W. Yan, H. Peng, Y. Li, Z. Liu, S. Wang, Z. Chen, L. Xiao, Z. Bian, C. Huanga, *Nanoscale*, **2016**, 8, 10806.
[58] F. Igbari, M. Li, Y. Hu, Z.-K. Wang, L.-S. Liao, *J. Mater. Chem. A*, **2016**, 4, 1326.
[59] S. H. Lee, D. H. Lee, K. Lee, C. W. Lee, *Adv. Funct. Mater.*, **2005**, 15, 1495.

[60] K. H. Lee, B. J. Park, D. H. Song, I. J. Chin, H. J. Choi, *Polymer*, **2009**, 50, 4372.
[61] B. H. Lee, S. H. Park, H. Back, K. Lee, *Adv. Funct. Mater.*, **2011**, 21, 487.
[62] W. Rehman, D. P. McMeekin, J. B. Patel, R. L. Milot, M. B. Johnston, H. J. Snaith, L. M. Herz, *Energy Environ. Sci.*, **2017**, 10, 361.
[63] M. Saliba, T. Matsui, J. Y. Seo, K. Domanski, J. P. Correa-Baena, M. K. Nazeeruddin, S. M. Zakeeruddin, W. Tress, A. Abate, A. Hagfeldt, M. Grätzel, *Energy Environ. Sci.*, **2016**, 9, 1989.
[64] T. J. Jacobsson, J. P. Correa-Baena, E. Halvani Anaraki, B. Philippe, S. D. Stranks, M. E. F. Bouduban, W. Tress, K. Schenk, J. Teuscher, J. E. Moser, H. Rensmo, A. Hagfeldt, *J. Am. Chem. Soc.*, **2016**, 138, 10331.
[65] S. Yue, K. Liu, R. Xu, M. Li, M. Azam, K. Ren, J. Liu, Y. Sun, Z. Wang, D. Cao, X. Yan, S. Qu, Y. Lei, Z. Wang, *Energy Environ. Sci.*, **2017**, 10, 2570.
[66] O. Abdulrazzaq, S. E. Bourdo, V. Saini, V. G. Bairi, E. Dervishi , T. Viswanathan, Z. A. Nima, A. S. Biris, *Energy Technol.*, **2013**, 1, 463.
[67] O. Abdulrazzaq, S. E. Bourdo, M. Woo, V. Saini, B. C. Berry, A. Ghosh, A. S. Biris, *ACS Appl. Mater. Interfaces*, **2015**, 7, 27667.
[68] J. Peng, Y. Wu, W. Ye, D. A. Jacobs, H. Shen, X. Fu, Y. Wan, T. Duong, N. Wu, C. Barugkin, H. T. Nguyen, D. Zhong, J. Li, T. Lu, Y. Liu, M. N. Lockrey, K. J. Weber, K. R. Catchpole, T. P. White, *Energy Environ. Sci.*, **2017**, 10, 1792.
[69] S. Song, G. Kang, L. Pyeon, C. Lim, G. Y. Lee, T. Park, J. Choi, *ACS Energy Lett.*, **2017**, 2, 2667.
[70] D. Liu, Y. Li, J. Yuan, Q. Hong, G. Shi, D. Yuan, J. Wei, C. Huang, J. Tang, M. K. Fung, *J. Mater. Chem. A*, **2017**, 5, 5701.

[71] X. Hu, Z. Huang, X. Zhou, P. Li, Y. Wang, Z. Huang, M. Su, W. Ren, F. Li, M. Li, Y. Chen, Y. Song, *Adv. Mater.*, **2017**, 29, 1703236.
[72] G. Kakavelakis, T. Maksudov, D. Konios, I. Paradisanos, G. Kioseoglou, E. Stratakis, E. Kymakis, *Adv. Energy Mater.*, **2017**, 7, 1602120.
[73] L. Zhu, J. Shi, S. Lv, Y. Yang, X. Xu, Y. Xu, J. Xiao, H. Wu, Y. Luo, D. Li, Q. Meng, *Nano Energy*, **2015**, 15, 540.
[74] H. Kim, J. Seo, N. Park, *ChemSusChem*, **2016**, 9, 2528.
[75] C.-H. Chiang, C.-G. Wu, *ChemSusChem*, **2016**, 9, 2666.
[76] Y. Yuan, J. Huang, *Acc. Chem Res.*, **2016**, 49, 286.
[77] C. Li, S. Tscheuschner, F. Paulus, P. E. Hopkinson, J. Kießling, A. Köhler, Y. Vaynzof, S. Huettner, *Adv. Mater.*, **2016**, 28, 2446.
[78] Z. Yu, B. Chen, P. Liu, C. Wang, C. Bu, N. Cheng, S. Bai, Y. Yan, X. Zhao, *Adv. Funct. Mater.*, **2016**, 26, 4866.
[79] L. Liang, Y. Cai, X. Li, M. K. Nazeeruddin, P. Gao, *Nano Energy*, **2018**, 52, 211.
[80] Y. Liu, Q. Chen, H.-S. Duan, H. Zhou, Y. Yang, H. Chen, S. Luo, T.-B. Song, L. Dou, Z. Hong, Y. Yang, *J. Mater. Chem. A*, **2015**, 3, 11940.
[81] N. Arora, M. I. Dar, A. Hinderhofer, N. Pellet, F. Schreiber, S. M. Zakeeruddin, M. Grätzel, *Science*, **2017**, 358, 768.
[82] K. Domanski, J.-P. Correa-Baena, N. Mine, M. K. Nazeeruddin, A. Abate, M. Saliba, W. Tress, A. Hagfeldt, M. Grätzel, *ACS Nano*, **2016**, 10, 6306.
[83] Z. Hawash, L. K. Ono, Y. Qi, *Adv. Mater. Interfaces*, **2018**, 5, 1700623.
[84] A. K. Jena, Y. Numata, M. Ikegami, T. Miyasaka, *J. Mater. Chem. A*, **2018**, 6, 2219.
[85] S. Kim, S. Bae, S.-W. Lee, K. Cho, K. D. Lee, H. Kim, S. Park, G. Kwon, S.-W. Ahn, H.-M. Lee, Y. Kang, H.-S. Lee, D. Kim,

Scientific Reports, **2017**, 7, 1200.

국문초록

유무기 하이브리드 페로브스카이트 물질을 기반으로 한 페로브스카이트 태양전지는 차세대 태양전지로 각광받으며 매우 빠르게 발달하였다. 페로브스카이트 광흡수층과 더불어 전하 전달층은 소자의 효율과 안정성을 결정하는 중요한 요소이다. 일반적으로, 유기 저분자, 전도성 고분자, 금속 산화물 반도체들이 전하 전달층으로 사용된다. 그 중 전도성 고분자는 여타의 반도체 소재와 차별화되는 장점으로 전하 전달층으로서 활발히 연구되고 있다. 전도성 고분자는 금속 산화물과는 달리 저온에서 박막으로 제조될 수 있어 플라스틱 기판에 사용하여 유연한 소자를 제조할 수 있다. 또한 용액 공정이 가능한 전도성 고분자는 스핀 코팅 혹은 스프레이와 같은 방법으로 쉽게 박막으로 제조될 수 있고, 유기 소분자와 비교하여서도 더 우수한 박막 형성 특성으로 인해 결함이 적고 얇은 박막으로 제조할 수 있다. 하지만 이러한 장점에도 불구하고, 지금까지 페로브스카이트 태양전지에서 주로 사용된 전도성 고분자는 그 가격이 상대적으로 비싸다는 단점이 있다.

폴리아닐린은 대표적인 전도성 고분자로 제조가 쉽고 전도도가 좋으며 환경적으로 안정하기 때문에 유기발광 다이오드, 염료감응형 태양전지, 전기변색소자, 센서소자 등에 널리 사용되고 있다. 특히, 폴리아닐린의 단량체인 아닐린은 폴리(3,4-에틸렌다이옥시싸이오펜), 폴리(3-헥실티오펜), 폴리트리아릴아민을 포함한 다른 전도성 고분자의 단량체보다 가격이 훨씬 저렴하다. 따라서 폴리아닐린은 페로브스카이트 태양전지의 전하 전달층 물질로 매우 큰 잠재력을 가지고 있다. 폴리아닐린의 전하 전달층으로의 응용이 몇몇의 논문을 통해 보고되긴 하였으나, 소자의 효율이 낮고 제조 과정이 복잡하거나 일반적인 페로브스카이트 태양전지의 형태를 갖지 않아 재현성이 떨어진다.

본 논문에서는 폴리아닐린 기반의 전하 전달물질을 제조하고 각기 다른 형태의 페로브스카이트 태양전지 내 전하 전달층으로 응용하는 방법을 제시한다. 용액 공정이 가능한 폴리아닐린 분산 용액이 제조되었으며, 역구조와 탄소전극기반의 페로브스카이트 태양전지 내 홀 전달층으로 사용되었다. 첫 번째로, 물에 분산된 폴리아닐린:폴리(스티렌 술포네이트)를 제조하고 홀 전달능력을 향상시키기 위해 계면활성제를 첨가하여 그 특성 변화를 유도하였다.

계면활성제로 인해 향상된 기판에 대한 젖음성과 홀 전달에 유리한 표면 조성으로 인해 소자의 광전변환효율이 향상되었다. 두 번째로, 캄포르술폰산에 의해 도핑된 폴리아닐린을 홀 전달층으로 사용한 페로브스카이트 태양전지를 제조하고 그 성능을 가장 흔히 사용되는 홀 전달층인 폴리(3,4-에틸렌다이옥시싸이오펜):폴리(스티렌 술포네이트)을 사용한 소자와 비교하였다. 폴리아닐린을 사용한 경우 더 높은 전도도와 전하 이동도로 인하여 홀 전달능력이 우수하여 소자의 광전변환효율도 더 우수하였다. 또한 흡습성이 있는 기존 홀 전달층과는 달리 습기에 안정적인 폴리아닐린을 사용하여 소자의 대기에서의 안정성이 크게 향상되었다. 마지막으로, 캄포르술폰산에 의해 도핑된 폴리아닐린을 탄소전극을 사용한 페로브스카이트 태양전지 내 홀 전달층으로 응용하였다. 유기 용매에 분산된 폴리아닐린은 페로브스카이트 박막 위에 코팅되어도 분해를 일으키지 않으므로 페로브스카이트층 위에 코팅될 수 있다. 따라서 페로브스카이트/탄소전극 사이에 코팅된 폴리아닐린 층은 계면에서 발생하는 전하 재결합을 효과적으로 방지하여 소자의 광전변환효율을 향상시켰다. 습기와 열에 안정적인 폴리아닐린과 탄소전극에 의해 대기, 열 안정성이 매우

뛰어난 페로브스카이트 태양전지가 제조되었다. 제조된 폴리아닐린 전하 전달물질은 전하 전달능력이 좋으며, 안정적이고, 다양한 응용이 가능하였다. 따라서, 본 논문은 저렴하며 효율적이고, 안정적이며 유연한 페로브스카이트 태양전지를 달성할 수 있는 홀 전달물질로서 전도성 고분자 폴리아닐린의 제조 및 응용에 대한 접근법을 제시한다.

주요어: 페로브스카이트 태양전지, 전도성 고분자, 폴리아닐린, 홀 전달물질, 탄소전극

학 번: 2016-30234